Engineering Structures 334 (2025) 120257

Contents lists available at ScienceDirect

Engineering Structures

journal homepage: www.elsevier.com/locate/engstruct

Mechanical behaviors of hybrid fiber-rebar reinforced concrete lining under ground surcharge loads—3D numerical simulation combined with full-scale test

Xiaohua Bao [a,b], Yingpeng Li [a,b], Xuehui Zhang [c,d,*], Xianlong Wu [a,b], Xiangsheng Chen [a], Hongzhi Cui [a,b]

[a] State Key Laboratory of Intelligent Geotechnics and Tunnelling, College of Civil and Transportation Engineering, Shenzhen University, Shenzhen, Guangdong 518060, China
[b] Key Laboratory of Coastal Urban Resilient Infrastructures (Shenzhen University), Ministry of Education, Shenzhen 518060, China
[c] Department of Civil and Environmental Engineering, The Hong Kong Polytechnic University, Hung Hom, Kowloon, Hong Kong SAR
[d] Geo-Engineering Section, Department of Geo-science and Engineering, Delft University of Technology, Delft, the Netherlands

ARTICLE INFO

Keywords:
Hybrid fiber-reinforced concrete (HFRC)
Segment ring
Shield tunnel
Nonlinear numerical analysis
Structural behavior

ABSTRACT

Traditional reinforced concrete (RC) segments used in shield tunnel linings face limitations in crack resistance and durability, while hybrid fiber-reinforced concrete (HFRC) offers a promising solution to enhance its long-term performance. However, significant knowledge gaps remain regarding the application of HFRC in conjunction with steel reinforcement rebars to improve the structural performance of segmental linings. This study examines the mechanical performance of tunnel linings constructed using four types of segments, namely traditional RC, unreinforced HFRC (UR-HFRC), partially reinforced HFRC (PR-HFRC), and fully reinforced HFRC (FR-HFRC). A refined three-dimensional finite element model (3D FEM) was developed, incorporating a constitutive model for HFRC derived from laboratory tests. The accuracy of the 3D FEM was validated against full-scale load test results. Key findings include: the FR-HFRC segment ring demonstrates the highest ultimate bearing capacity and enhances subsequent stiffness during the hardening phase compared to RC segments. In reinforced segments (RC, PR-HFRC, FR-HFRC), rebars effectively mitigate cross-sectional yielding; however, this advantage comes at the cost of successive plastic hinge formation at segment joints during ultimate failure. Both bolts and reinforcement play a crucial role in load distribution, with HFRC enhancing the synergy between bolts and segments, thereby reducing reinforcement stress levels. Nevertheless, the stress in the reinforcement rarely reaches the yield point, suggesting potential underutilization in certain cases. By optimizing material configurations, HFRC can potentially offer an efficient and cost-effective solution for tunnel lining construction.

1. Introduction

1.1. Concrete segmental lining of shield tunnel

Underground tunnel infrastructure plays a critical role in modern urban development. These tunnel structures expand usable underground space, alleviating surface traffic congestion, and enhance urban resilience to unforeseen natural disasters [1–4]. Among the various tunnel construction methods, the shield tunneling method (or boring method) has emerged as one of the most widely used techniques, particularly in urban tunnel projects due to its advantages of ground disturbance control and reduced labor requirements. Shield tunnels typically utilize segmented linings, with reinforced concrete segments prefabricated and assembled into rings on-site to withstand both internal and external loads. The structural behavior and durability of these segmental linings are critical factors in ensuring the long-term operational safety of tunnel infrastructure.

Currently, traditional reinforced concrete (RC) segments are the predominant type used for constructing shield tunnels [5]. While RC segmental linings have been widely adopted in tunnel projects, they have exhibited several issues as their service life progresses [6–8]. Over time, RC is prone to cracking [9,10], steel bar corrosion [11], and subsequent leakage [12,13], particularly in groundwater environments where water infiltration accelerates reinforcement corrosion,

* Corresponding author at: Department of Civil and Environmental Engineering, The Hong Kong Polytechnic University, Hung Hom, Kowloon, Hong Kong SAR.
E-mail address: xuehzhang@polyu.edu.hk (X. Zhang).

https://doi.org/10.1016/j.engstruct.2025.120257
Received 24 December 2024; Received in revised form 13 March 2025; Accepted 31 March 2025
Available online 10 April 2025

significantly compromising the durability of tunnel linings. For instance, the Chamshir water conveyance tunnel in Iran has been reported to experience severe RC-related issues, including lining concrete spalling, corner chipping, and center crumbling [14]. Moreover, the relatively low tensile strength of RC segments renders them vulnerable to tension cracks induced by ground surcharge and dynamic loads [15]. Additionally, grout voids beneath the tunnel lining can lead to significant stress concentrations, resulting in segment cracking and damage [16]. As the demand for enhanced crack resistance and durability in tunnel structures grows, RC segments reveal significant limitations in these critical aspects [17]. Therefore, it is essential to explore alternative segment types, preferably those with superior crack resistance, to improve the serviceability and durability of tunnel infrastructure.

1.2. Performance of FRC segments

Fiber-reinforced concrete (FRC) is a composite construction material created by uniformly dispersing short fibers within plain concrete [18,19]. The most commonly used fibers include steel fibers and synthetic fibers [20]. When two or more types of fibers are combined in FRC, the material is referred to as hybrid fiber-reinforced concrete (HFRC), which exhibits potential to outperform single-fiber reinforced concrete when at proper hybrid fiber mixing ratios. HFRC leverages the synergistic effects of different fiber types, resulting in significant improvements in material properties [21,22]. FRC has shown exceptional effectiveness in enhancing the crack resistance, ductility, and durability of tunnel linings, making it an area of increasing interest among researchers [23].

Previous experimental and numerical studies have confirmed the potential of FRC in tunnel segments [24–28]. In terms of structural mechanical performance, the incorporation of FRC enhances the cracking resistance and toughness of tunnel segments, improving their ability to withstand high concentrated loads. For example, Meng et al. [29] demonstrated through full-scale segment load tests that the combination of steel fibers and conventional reinforcement (steel rebars) significantly improves cracking resistance and load-bearing capacity. Additionally, steel fibers have been shown to compensate for the loss in cracking resistance and structural toughness in concrete elements, even when the reinforcement ratio is reduced [30]. For instance, Conforti et al. [31] conducted an experimental study and found that when combined with a minimal amount of conventional rebars, synthetic fibers can still ensure adequate load-bearing capacity of tunnel segments. Gholami et al. [32] and Trabucchi et al. [33] numerically simulated the mechanical response of individual FRC segments subjected to highly concentrated forces from the hydraulic cylinders of a shield machine during the tunneling process. Their findings revealed that the grade of FRC (according to the fib Model Code 2010 [34]) significantly influences the segment's ability to resist cracking. Overall, previous studies confirm the effectiveness of FRC in enhancing the crack resistance and performance of segments in shield tunnel structures [35–40]. Despite the substantial potential of FRC in precast segment structures, research on the overall mechanical behaviors of ring structures remains notably less extensive compared to RC segments.

Most experimental studies on FRC segments are limited to the scale of individual segments [41–44]. The results obtained from individual segment tests cannot fully capture the structural performance of the entire lining ring. Therefore, it is essential to analyze the performance from the perspective of the entire ring structure. The use of FRC offers the potential for optimizing structural design parameters, which can reduce reinforcement requirements, lower construction costs, and enhance durability [25]. However, the effectiveness of these optimization strategies is closely tied to variations in reinforcement ratios within FRC segments [45]. Although it is essential to investigate the impact of various combinations of fibers and reinforcement rebars on the structural properties of tunnel linings, research in this area remains limited due to the high cost and complex loading conditions associated with full-scale ring tests, which pose significant challenges for implementation. As a more cost-effective and efficient alternative, numerical simulations offer a practical approach to studying the performance of three-dimensional lining structures, thus gaining increasing attention from researchers. A carefully validated numerical model can accurately characterize structural behavior [46–49]. For instance, the simplified numerical model developed by Liu et al. [50] was used to preliminarily analyze the structural performance of FRC segments. However, due to the complexity of the segment structure, details such as hand holes and bolts were not fully represented in these studies. Therefore, conducting more detailed numerical simulations, validated by full-scale ring tests, with a particular focus on the mechanical properties of FRC under different reinforcement ratios, will provide valuable insights for the practical application of FRC segments in engineering.

1.3. Contributions and innovations in this study

In this study, HFRC is utilized, incorporating both macro hooked-end steel fibers and micro straight steel fibers. To address the mechanical performance directly related to the practical application of HFRC in tunnel structures, a comprehensive numerical study on the overall mechanical behavior of FRC segmental rings is conducted, with model verification achieved through a full-scale laboratory load test. The innovations of this study are threefold: (1) Instead of focusing on a single type of FRC segment lining, this study expands the analysis to investigate the mechanical properties of tunnel linings made of four different segment types: traditional reinforced concrete (RC), unreinforced HFRC (UR-HFRC), partially reinforced HFRC (PR-HFRC), and fully reinforced HFRC (FR-HFRC). The study evaluates key structural characteristics such as load-bearing capacity and stiffness; (2) A refined three-dimensional finite element model (3D FEM) is developed, which accurately models critical structural components, including bolts, manholes, and reinforcement, to reveal the mechanical behavior of HFRC segmental rings. This model was validated through comparison with results from a full-scale load test; (3) The simulation results specifically examine the influence of bolt connections (segment joints) on the overall performance and stress distribution of the lining structure under ultimate load conditions, and provide optimization recommendations for the practical design of HFRC segments.

2. Background engineering

2.1. Background project introduction

The Liyumen - Qianhaiwan interval tunnel of Shenzhen Metro Line 1 was constructed using the shield method. The tunnel is 710 m long and buried at depths ranging from 7 to 11 m, primarily passing through fully weathered granite and granite residual deposit layers. The large land reclamation project which resulted in a substantial surface backfilling (a maximum height of 25 m) on the site above the tunnel, as shown in Fig. 1(a), which further brings about considerable vertical overload to the in-service metro tunnel. Field observations reveal severe horizontal convergence deformation at several tunnel rings (see Fig. 1(b)), with significant resultant concrete damage including cracking and spalling especially at the tunnel joints (see Fig. 1(c)).

2.2. Overview of full-scale load test

To investigate the structural performance and failure modes of shield tunnels under surface surcharge load as illustrated in Fig. 1, a full-scale load test of segmental tunnel ring was conducted. The configuration of the full-scale test is shown in Fig. 2, while Fig. 2(a) presents an overall view of the loading platforms and Fig. 2(b) and (c) represent the external and bird view of the actual loading setup. A total of 24 loading points were arranged along the tunnel circumference: 6 points for P_1 (crown loading), 10 points for P_2 (waist loading), and 8 points for P_3 (shoulder loading). At each loading point, two hydraulic jacks plus a vertical load-

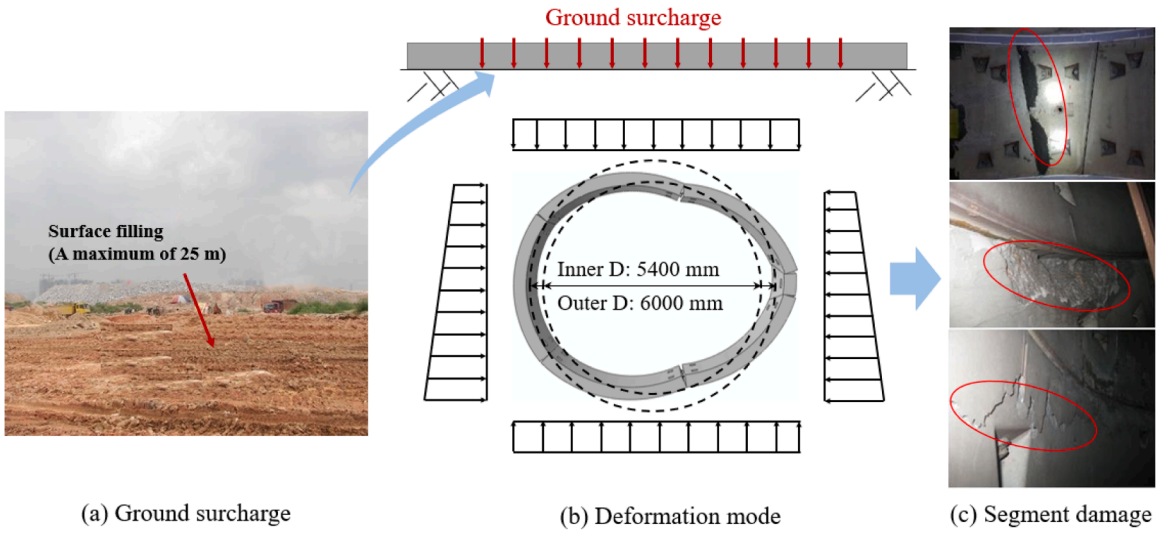

Fig. 1. Deformation patterns and damage of the shield tunnel subjected to high ground surcharge.

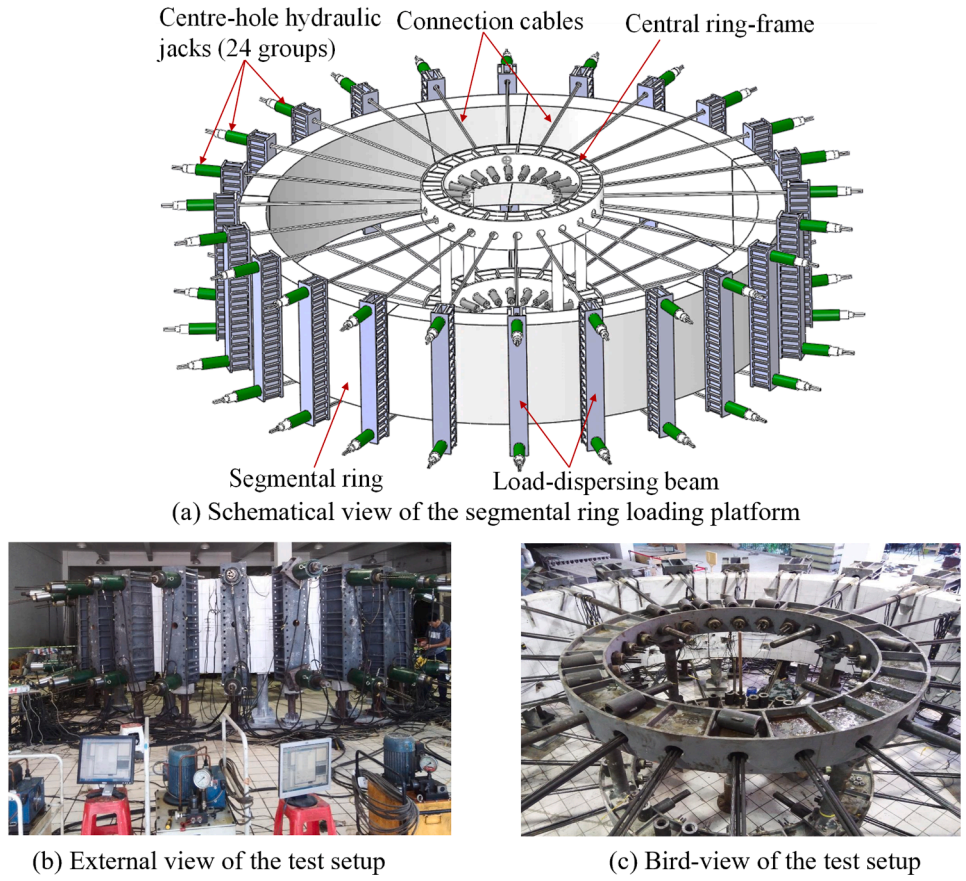

Fig. 2. Overview of the full-scale segmental ring test (based on Lu [51]).

dispersing beam are used to exert surface loading. More detailed of the loading conditions can be found in work by Lu [51]. The detailed test results will be interpreted in the following Section 3 and compared with the simulation results obtained from the 3D finite element simulation.

3. Three-dimension(3D) numerical simulation

3.1. Three-dimension (3D) finite element model

Fig. 3(a) illustrates the detailed construction of the finite element model (FEM), which is composed of six precast segments: three standard segments (B1, B2, and B3) with the central angle being 72°, two adjacent segments (L1 and L2) with the central angle being 64.5°, and one key segment (F) with the central angle being 15°. The outer diameter of the

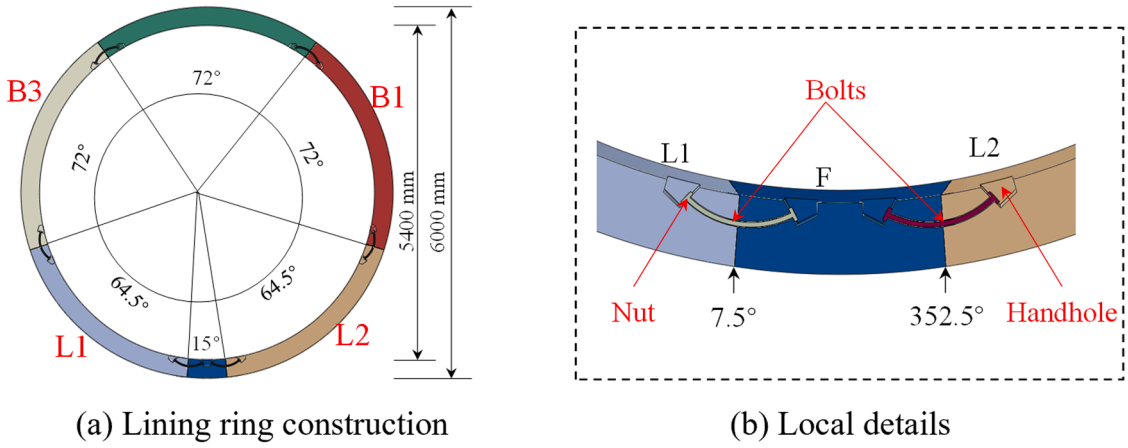

Fig. 3. Segmental ring structure.

lining ring is 6000 mm, and the inner diameter is 5400 mm, with a segment width of 1500 mm and a thickness of 300 mm. Along the circumference the segments are assembled and connected using two M24 type bolts with a bolt diameter of 24 mm and a tensile capacity of 8.8 GPa. The detailed information of the bolt connection is shown in Fig. 3(b). The FEM considers four types of segmental lining: RC (rebars only), UR-HFRC, PR-HFRC (reduced amount of circumferential rebars + fibers) with a reinforcement ratio of 0.79%, and FR-HFRC (sufficient circumferential rebars + fibers) with a circumferential reinforcement ratio of 1.58% based on the engineering project background. The reinforcement layout for both RC and FR-HFRC is identical, following the actual tunnel design in the Shenzhen Metro Line 1. In contrast, the PR-HFRC configuration uses only 50% of the specified reinforcement quantity while maintaining the same type of rebar. This is achieved by reducing a portion of the reinforcement rebar used, resulting in a reinforcement ratio of 0.79%.

Fig. 4 presents the overall 3D FEM utilized in this study. As depicted in Fig. 4(a), solid elements (C3D8R) are used to model the concrete and connecting bolts, while truss elements (T3D3) simulate the reinforcement rebars, as shown in Fig. 4(b). The numerical model incorporates essential components, including the rebar cage, connecting bolts, and handholes. Fig. 4(c) illustrates the segment with the handholes, and Fig. 4(d) shows the connecting bolts at joints. To simplify the modeling process, certain structural components such as sealing gaskets, joint grooves, and load transfer pads are excluded. After meshing, a total of 158,527 nodes and 139,600 elements are generated for subsequent numerical calculation.

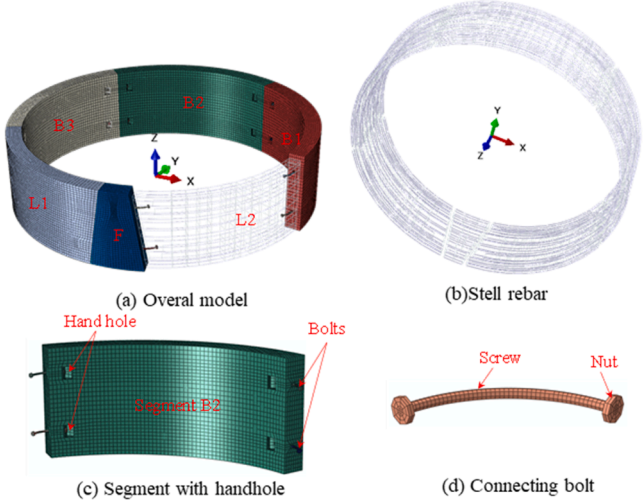

Fig. 4. Detailed 3D Finite Element Model of the segmental ring.

3.2. Material constitutive models and parameters

3.2.1. Constitutive parameters of concrete and steel

The concrete damage plasticity (CDP) model was used to simulate the nonlinear mechanical behavior of quasi-brittle materials like concrete, integrating damage mechanics and plasticity theory to capture stiffness degradation and irreversible deformations under loading. The model employs compressive (d_c) and tensile (d_t) damage factors to quantify stiffness reduction caused by compressive crushing and tensile cracking, respectively (see Fig. 5). Both factors range from 0 (undamaged) to 1 (fully damaged), evolving through equivalent plastic strains (ε_c^{in}, ε_t^{ck}), as shown in formulas (1)-(4). These damage variables interact with plastic strains to govern the stress-strain response, accounting for tension-compression asymmetry and irreversible unloading stiffness degradation. The coupling of damage and plasticity enables realistic representation of material softening, hysteresis, and path-dependent behavior under cyclic loading.

The tunnel lining is constructed using C50-grade concrete, with more details summarized in Table 1. The tensile and compressive stress-strain relationships were calculated according to the Chinese code for design of concrete structures [52] to determine the parameters of the CDP model, as shown in Fig. 6. The mechanical behavior of the steel was modeled using an ideal elastoplastic model, with a density of 7900 kg/m^3 , an elastic modulus of 200 GPa, and a Poisson's ratio of 0.3. The main rebar grade is HRB400, with a diameter of 18 mm, a yield strength of 400 MPa, and an ultimate strength of 500 MPa. Further, the yield strength of the M24 type connecting bolts is 640 MPa, with an ultimate strength of 800 MPa.

The constitutive relationship of the CDP model for concrete is shown as follows:

$$\sigma_t = (1 - d_t)E_0(\varepsilon_t - \varepsilon_t^{pl}) \tag{1}$$

$$\sigma_c = (1 - d_c)E_0(\varepsilon_c - \varepsilon_c^{pl}) \tag{2}$$

$$d_c = 1 - \frac{\sigma_c E_0^{-1}}{\sigma_c E_0^{-1} + \varepsilon_c^{in}(1 - 1/b_c)} \tag{3}$$

$$d_t = 1 - \frac{\sigma_t E_0^{-1}}{\sigma_t E_0^{-1} + \varepsilon_t^{ck}(1 - 1/b_t)} \tag{4}$$

where σ_c, σ_t, E_0 are the compressive strength, the tensile strength, and the secant modulus. ε_c^{pl}, ε_t^{pl}, ε_c^{in}, $\varepsilon_t^{ck}$are the compressive equivalent plastic strain, the tensile equivalent plastic strain, the inelastic strain, the inelastic strain. b_c and $b_t$take 0.7 and 0.1, respectively [53].

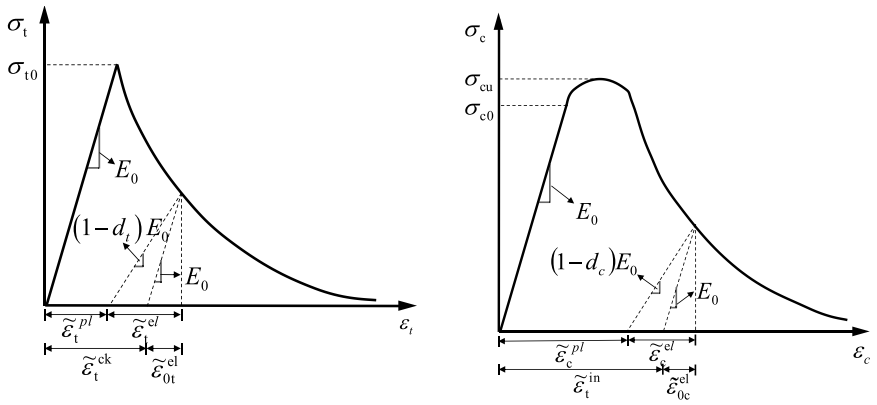

(a) Tensile stress-strain relationship (b) Compressive stress-strain relationship

Fig. 5. Description of CDP model: (a) tensile stress–strain curve of concrete; and (b) compressive stress–strain curve of concrete.

Table 1
Parameters of the CDP model for concrete.

Parameters	Value	Parameters	Value
Densityρ (kg/m^3)	2430	Eccentricity	0.1
Young's modulus E (GPa)	35.5	f_{b0}/f_{c0}	1.16
Poisson's ratio ν	0.167	Invariant stress ratio K_c	0.666667
Expansion angle ψ (°)	38	Viscosity parameters μ	0.0005
Uniaxial compressive strength represents value $f_{c,r}$(MPa)	32.4	Uniaxial tensile strength represents value$f_{t,r}$ (MPa)	3.27
Peak compressive strain of concrete $\varepsilon_{c,r}(10^{-6})$	1640	Peak tensile strain of concrete$\varepsilon_{t,r}(10^{-6})$	128
Parameter values of the descending section of the stress-strain curve of the compression curve α_c	1.36	Parameter values of the descending section of the tensile stress-strain curve α_t	3.82
Compressive strain of concrete when the stress of descending section is 0.5·$f_{c,r}$ $\varepsilon_{cu}(10^{-6})$	3772		

3.2.2. *Hybrid fiber-reinforced concrete (HFRC) constitutive model and verification*

According to previous studies [54–56], the optimal fiber types and dosages suitable for HFRC in tunnel segment were determined as follows: the macro hooked steel fibers have a volume fraction of 0.3 %, while the micro straight steel fibers have a volume fraction of 0.2 %. Table 2 summarizes the physical and mechanical properties of the used fibers. The CDP model was used to simulate HFRC. The compressive stress-strain parameters of the CDP model of HFRC can be acquired using the standards for ordinary concrete [34], while the tensile stress-strain parameters are determined according to the manual "RILEM-TC-162-TDF" [57]. Fig. 7 illustrates the tensile stress-strain relationship of HFRC, where f_{R1} and f_{R4} represent the residual flexural strength parameters which should be obtained from notched beam tests. From a notch beam test (see Fig. 8(a)) the f_{R1} and f_{R4} are determined as 4.51 MPa and 4.12 MPa, respectively. The corresponding beam FEM has been established (see Fig. 8(b)), and Fig. 8(c) presents the load-crack mouth opening displacement (CMOD) curves derived from both numerical simulations and experimental notch beam tests. A comparison reveals that the numerical results closely match the experimental data, successfully reproducing the cracking characteristics of HFRC under a three-point flexural test.

Table 2
Physical and mechanical properties of long hooked-end steel fibres and short straight steel fibres.

Fibre Type	Length (mm)	Diameter (mm)	Aspect ratio	Elasticity modulus (GPa)	Tensile strength (MPa)
Long hooked-end steel fibre	50	0.75	67	200	1500
Short straight steel fibre	13	0.2	65	200	2788

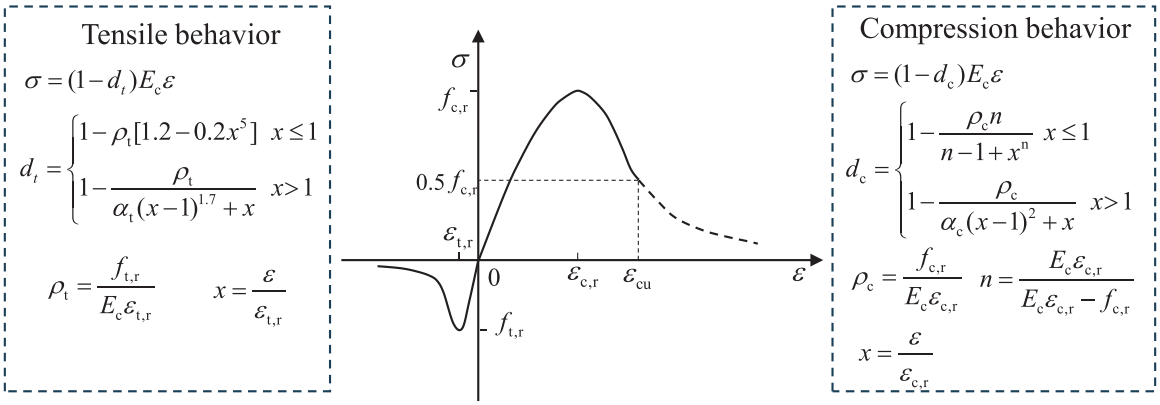

Fig. 6. Uniaxial stress-strain curve for plain concrete in Chinese code [52].

$$\sigma_1 = 0.7 f_{fctm,fl}\,(1.6-d) \qquad \epsilon_1 = \sigma_1 / E_c$$
$$\sigma_2 = 0.45 f_{R,1} \kappa_h \qquad \epsilon_2 = \epsilon_1 + 0.1‰$$
$$\sigma_3 = 0.37 f_{R,4} \kappa_h \qquad \epsilon_3 = 25‰$$
$$E_c = 9500 (f_{fcm})^{1/3}$$
κ_h : size factor
$$\kappa_h = 1.0 - 0.6 \cdot \frac{h[\mathrm{cm}] - 12.5}{47.5} \quad | \; 12.5 \le h \le 60[\mathrm{cm}]$$

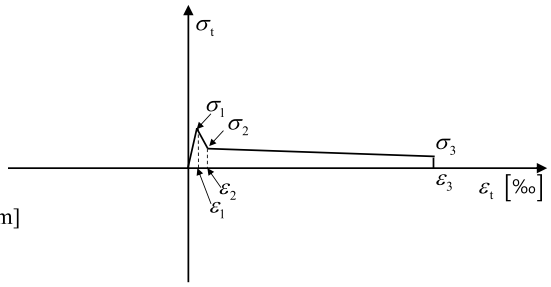

Fig. 7. Uniaxial tensile stress-strain curve of concrete for FRC.

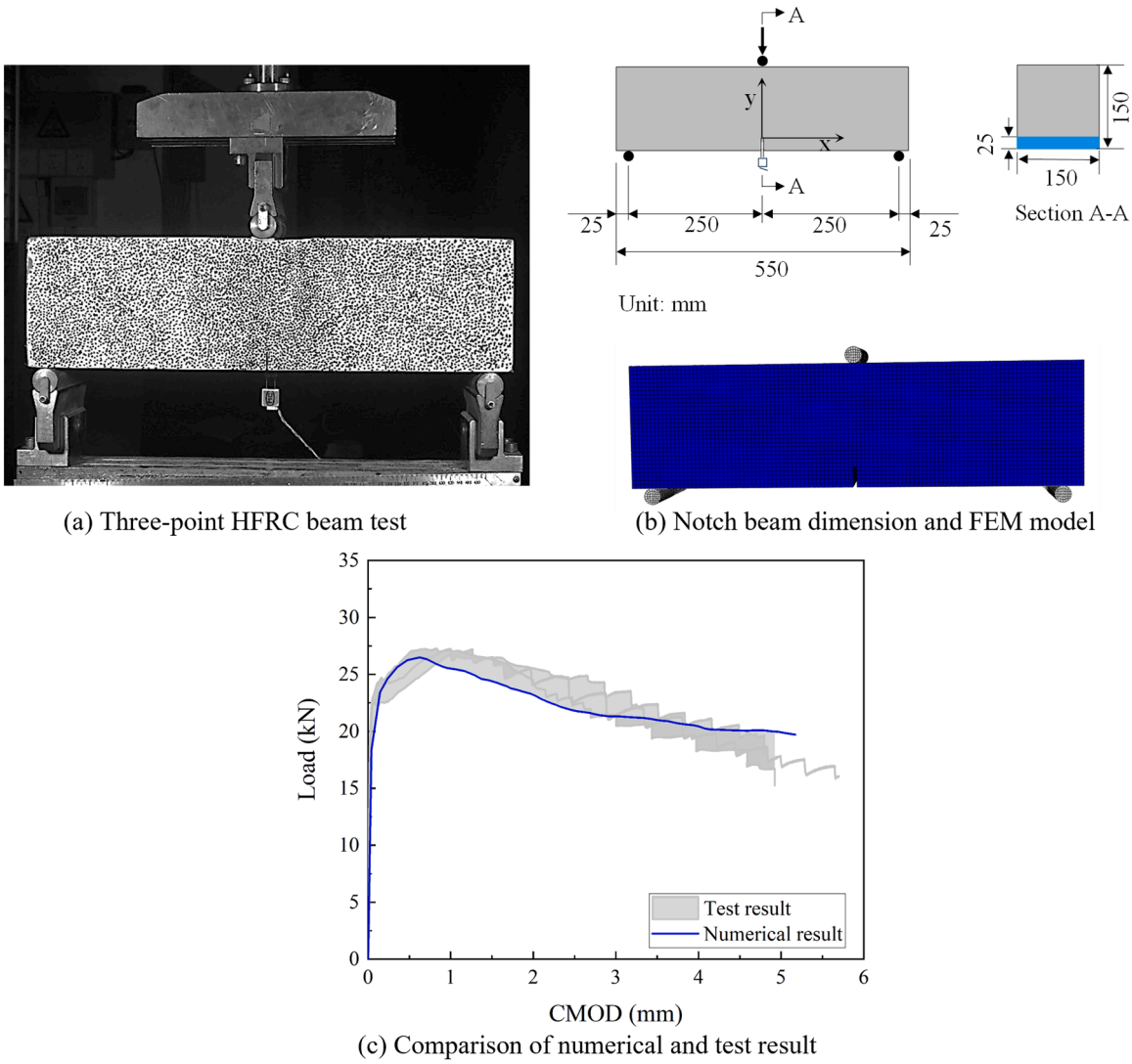

Fig. 8. Notch HFRC beam test and numerical modelling for stress-strain parameter determination.

3.3. Interactions and boundary settings

The boundary conditions of the 3D FEM are illustrated in Fig. 9, where the top and bottom surfaces of the lining ring are set as supported by rollers in the Z-direction, namely the out-of-plane movement is restricted (shown in Fig. 9(a)). Along the ring circumference, the displacements in the X-direction at the 0° and 180° positions are fixed. At angles of 90° and 270°, the displacements in the Y-direction are also fixed. Fig. 9(b) shows the joint interaction between two adjoining segments, which is modeled using surface-to-surface contact with finite sliding and face-to-face contact. The interface contact properties are defined for both tangential and normal behaviors using penalty functions and hard contact, with a friction coefficient set at 0.5 and a maximum elastic slip of 0.005 [58, 59] at segment joint interface. The bolt surface and the segment also adopt a surface-to-surface contact, with a friction coefficient set at 0.3 and a maximum elastic slip of 0.005 [58]. The tie constraints are applied between nut end face and the handhole surface. Additionally, the prestress of bolt is neglected. The interaction between the steel rebar and concrete is simulated by embedded constraints.

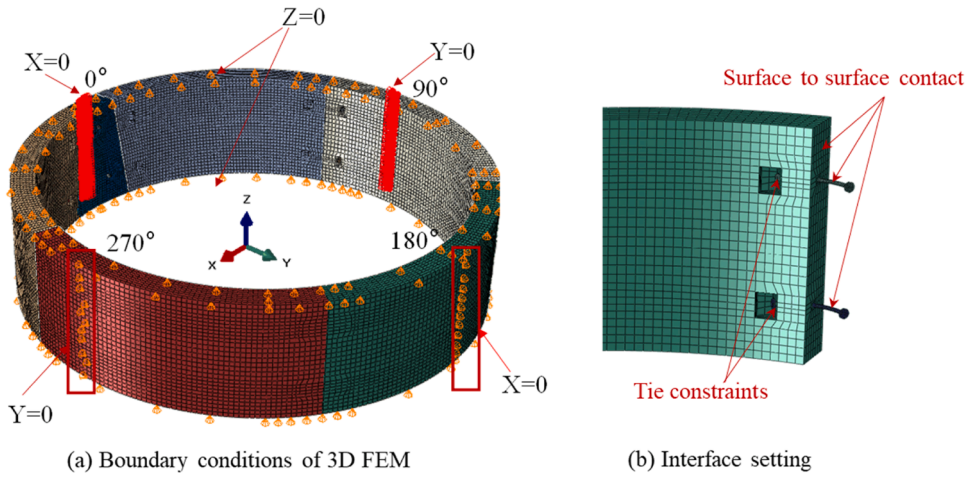

(a) Boundary conditions of 3D FEM (b) Interface setting

Fig. 9. Boundary conditions and interactions.

3.4. Model accuracy validation

The suitability and accuracy of the 3D FEM are first validated by comparing the simulation results with the full-scale test of an RC segmental ring. Fig. 10 provides the test and FEM results of the horizontal convergence deformation and the joint opening at 216°. As shown in Fig. 10(a), the computed horizontal convergence deformation (Δd) closely aligns with the full-scale test results. Fig. 10(b) illustrates the joint opening displacement at 216°, demonstrating a good agreement between the simulation and test results. It is worth noting that during the initial loading phase both the horizontal convergence and joint opening measurements observed in the tests are slightly higher than the calculated values. This discrepancy can be attributed to neglecting the effects of soft sealing gaskets and cushion pads at joints in the numerical simulation. In the full-scale tests, these components deform easily even from the initial loading steps, whereas in the FEM, the direct hard contact of segments at joints exhibits a higher stiffness and therefore a slightly smaller deformation level.

3.5. Loading procedure

Based on the validated 3D FEM, the subsequent numerical simulations focus on investigating the mechanical response of tunnel ring linings made of four types of segments under the negative impacts of ground surcharge as exemplified in the background engineering. The loading path of the numerical model is established as follows: the locations of the 24 loading points remain unchanged from those in the full-scale test, with the distributed load on the tunnel being equivalent to a point load (see Fig. 11(a)). According to the literature [47, 60], each loading point can be shown by formula (5)-(7).

$$P_1 = \gamma HBL \tag{5}$$

$$P_2 = P_1 K \tag{6}$$

$$P_3 = 0.5\times(P_1 + P_2) \tag{7}$$

where P_1 and P_2 are the vault and waist load; γ is the average soil weight, as 17.8 kN/m^3; H is the tunnel depth; B is the width of segment ring; L is the load arc range simulated by a single set of jacks at the tunnel vault; K is the coefficient of lateral pressure of soil determined as 0.7 in this study.

As shown in Fig. 11, the entire loading process is divided into four stages: (1) at the first stage, P_1 is initially increased to 20 kN and then gradually loaded to 95 kN, with each increment of 15 kN per step, while

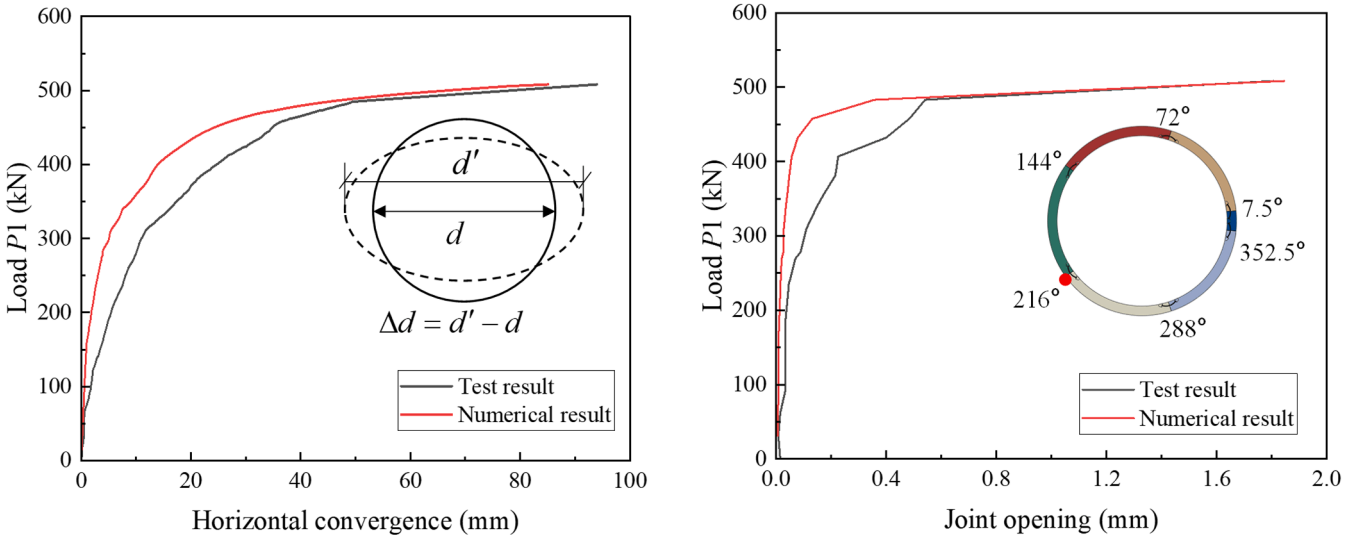

(a) Horizontal convergence deformation (b) Joint opening at 216°

Fig. 10. Comparison of numerical results with test results.

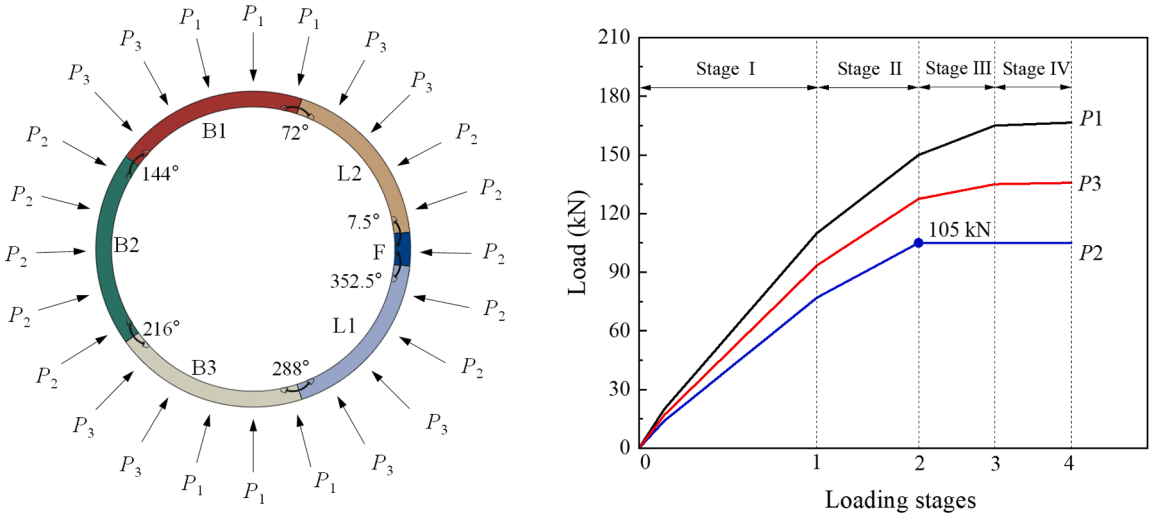

(a) Load point distribution (b) Load time-history curve

Fig. 11. Loading procedure settings in the FEM simulation.

maintaining $P_2 = 0.7 \bullet P_1$. (2) at the second stage, P_1 is increased from 95 kN by an increment of 10 kN until reaching 150 kN, with P_2 remaining the same portion of P_1 as in the first stage; (3) at the third stage, P_1 is incrementally increased by 5 kN until reaching 165 kN, keeping P_2 constant; (4) at the fourth stage, P_1 is further increased by 0.5 kN while maintaining P_2 constant until the structure fails completely. To better describe the structural stress state with surcharge loads, a generalized load P is defined as $P = P_1 - P_2$ and further used for the result interpretation.

4. Simulation results analysis

4.1. Structural internal forces and crack evolution

To gain an overview of the full behavior process of the tunnel lining, the deformation behaviors and failure modes of a UR-HFRC segmental ring is firstly demonstrated. Fig. 12(a) illustrates the deformation evolution time-history of the UR-HFRC segmental ring, which can be roughly divided into four phases: (1) Phase-1 indicates the elastic deformation phase. Initially, as the load increases, the structure experiences minimal deformation until the first tensile crack appears at 7.5°, marking the elastic limit of the structure; (2) Phase-2 is the elastoplastic deformation phase, where although the load increments are small, the structural deformation continues, leading to the onset of plastic deformation. During this phase, localized compressive yielding occurs in the segment concrete, and the structure reaches its elastic-plastic limit; (3) Phase-3 represents the structure hardening phase, where the yielding of partial concrete cross-sections and bolts triggers a redistribution of internal forces within the structure and a resultant raising bearing capacity, reaching the bearing capacity limit and yielding occurs at the bolts of joints and segment; (4) finally, Phase-4 is the ultimate failure phase where horizontal convergence deformation rapidly expands but without a significant increase in load, leading to a final loss of structural stability.

It is noteworthy that in phase 3, following local concrete crushing, the enhanced load-bearing capacity of the lining structure is predominantly attributed to the structural integrity and the effective redistribution of internal stresses. Steel bars or fibers at cracks provide tensile

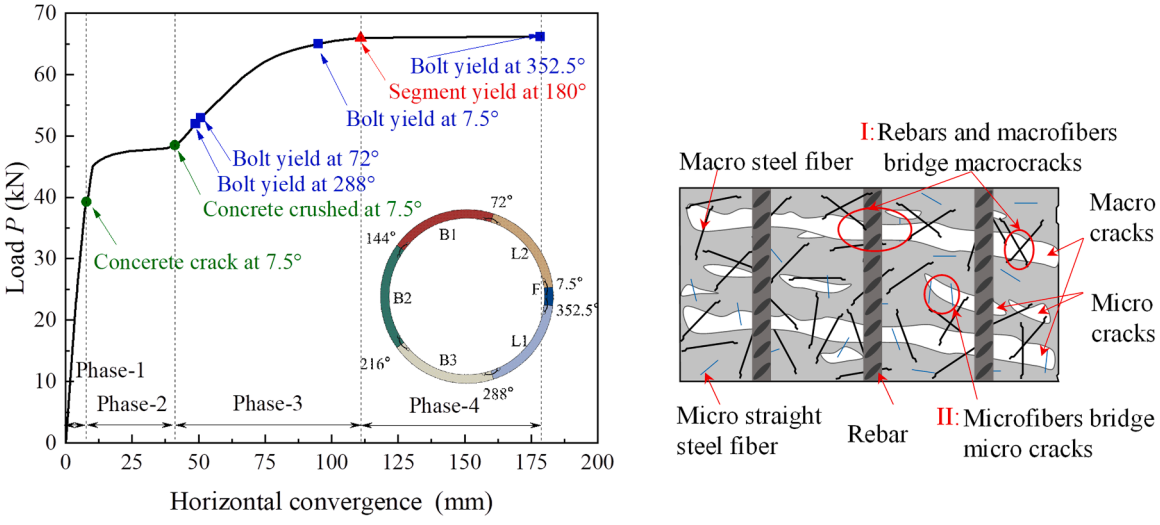

(a) Load point distribution (b) Load time-history curve

Fig. 12. Structural deformation evolution process of UR-HFRC segmental ring.

and shear resistance, transferring internal forces from cracked concrete to limit crack propagation and maintain structural integrity (see Fig. 12 (b)). Additionally, bolts at joints bear increased loads after concrete crushing, absorbing energy through deformation and delaying structural failure.

The crack propagation in the segmental ring during the loading process is illustrated in Fig. 13. DAMAGET (an Abaqus output variable category [61]) serves as a damage parameter (d_t) within the CDP model to quantify material degradation caused by crack initiation and propagation. Previous studies have demonstrated that tensile damage indicators, such as DAMAGET, provide a reliable metric for assessing crack occurrence and evolution in concrete structures [62, 63]. Overall, a limited number of cracks occur through the elastoplastic phase (Phase-2), whereas significant crack propagation mainly occurs during the hardening phase (Phase-3) and the ultimate failure phase (Phase-4). As shown in Fig. 13(a), for the RC segment, a through crack first appears on the outer circumference surface (B2) at $P = 45$ kN; within the range of $45 \leq P < 55$ kN, the crack propagates slowly, but once $P1$ exceeds 55 kN, the crack rapidly extends with increasing load. Fig. 13(b) depicts the crack propagation process for the UR-HFRC segment, which exhibits a higher cracking load (48 kN) than that of RC. Furthermore, at the same load level the number of tensile cracks near the joints at 72° and 288° is fewer in UR-HFRC lining compared to that of the RC lining. This suggests that, in the absence of reinforcement rebars, UR-HFRC's lower stiffness reduces stress concentration at the joints while leveraging the energy absorption of HFRC during cracking. Fig. 13(c) and (d) demonstrate that the combination of reinforcement rebars and HFRC significantly reduces crack formation; the FR-HFRC segment ring exhibits only a few cracks upon reaching the bearing capacity limit. However, the use of FR-HFRC may lead to material wastage, as the potential capacity of both reinforcement and HFRC is not fully realized.

To quantitatively assess the damage degree of the segment ring, the number of damaged elements (N_s) is counted by checking a threshold of DAMAGET result exceeding 0.9. It is evident from Fig. 14 that the three types of HFRC segment rings exhibit a significantly lower N_s the during loading process compared to RC segment. It is noteworthy that the N_s decreases by 6 % only between FR-HFRC and PR-HFRC segment rings. This suggests that increasing the usage of rebars in HFRC segments does not significantly contribute to a reduction in damaged areas of the segmental ring. Therefore, through the reasonable configuration of conventional reinforcement rebars and HFRC, the crack resistance of segmental lining can be significantly improved, and HFRC potentially

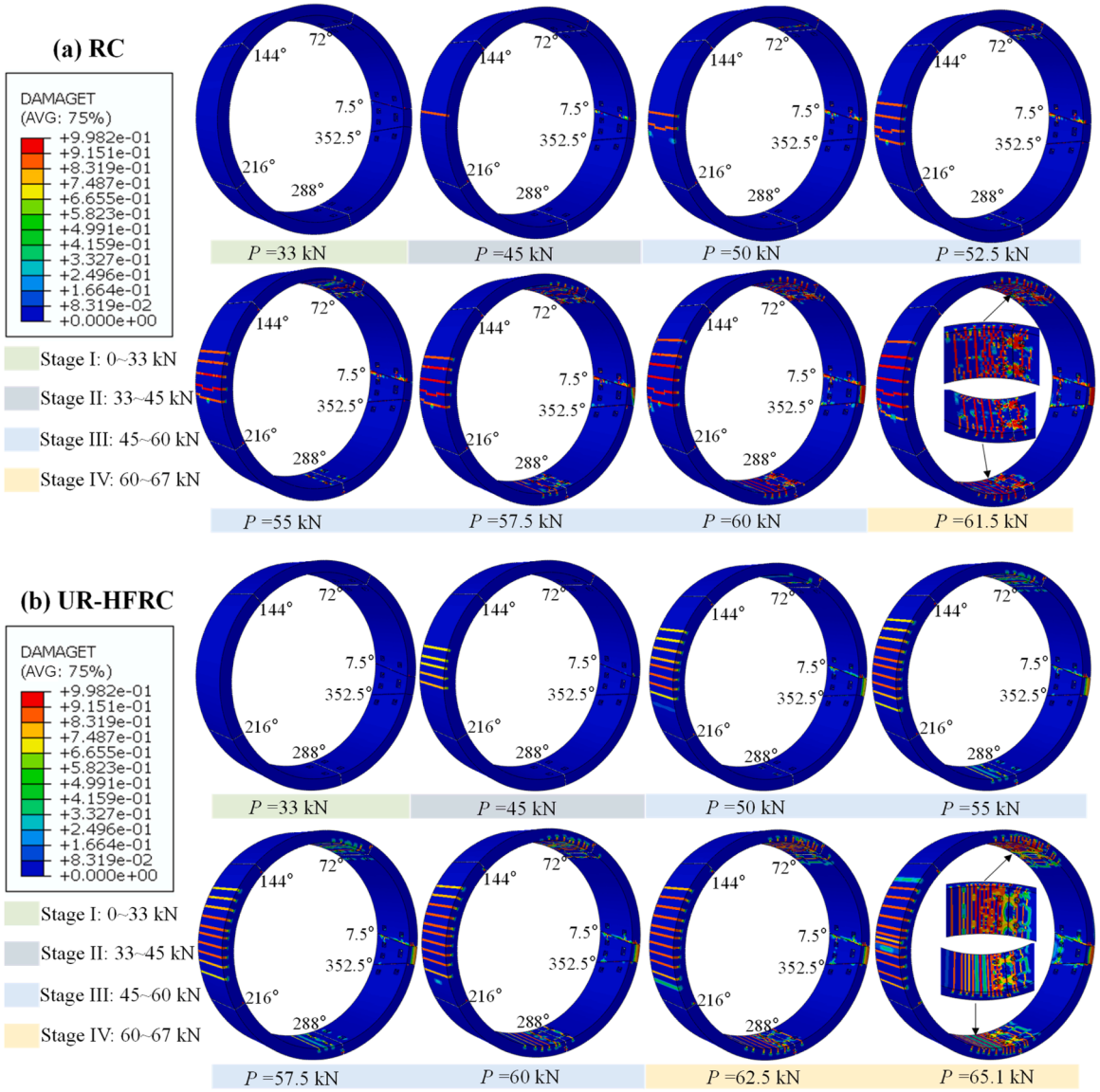

Fig. 13. Crack propagation process of segment concrete.

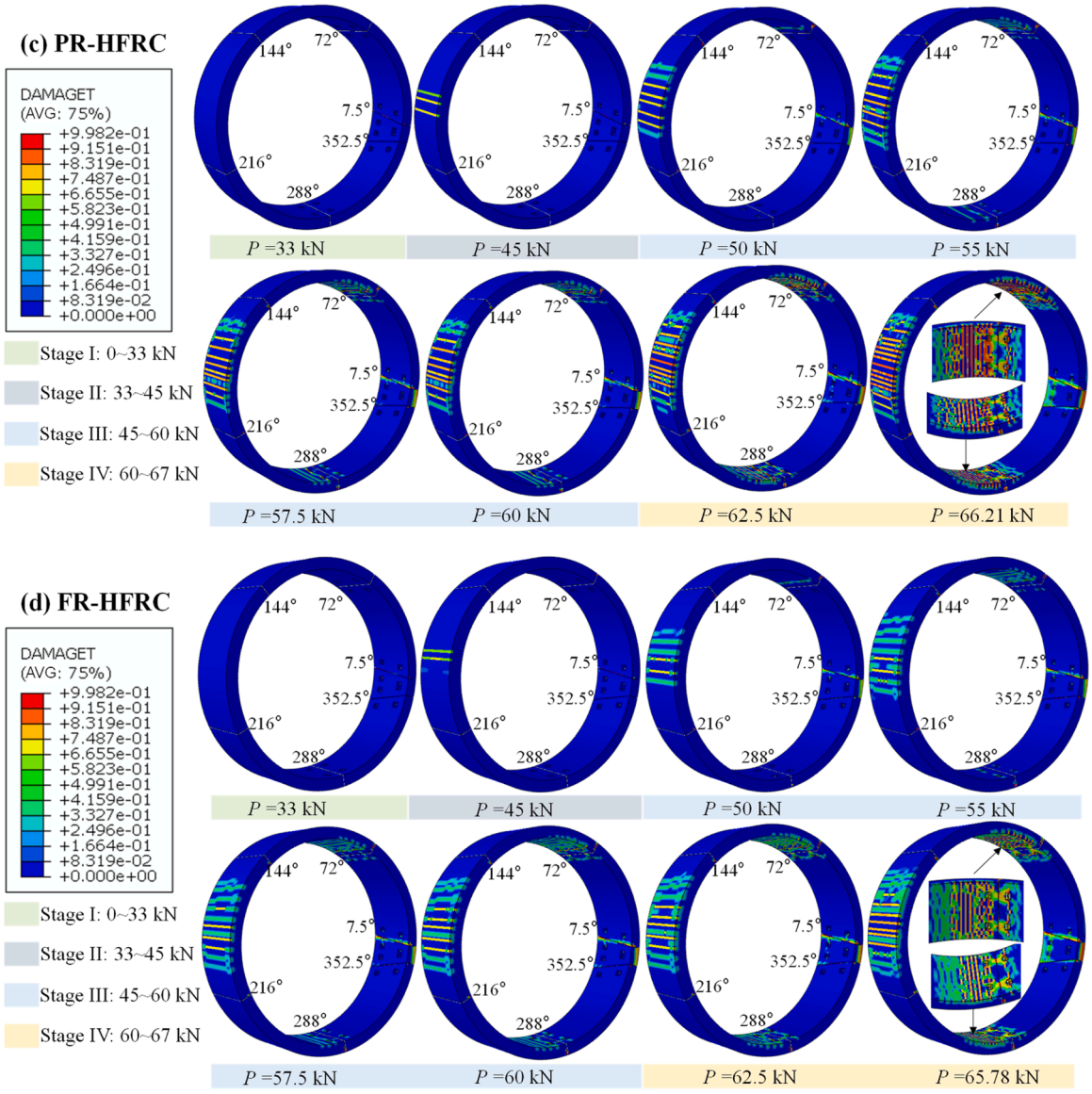

Fig. 13. (*continued*).

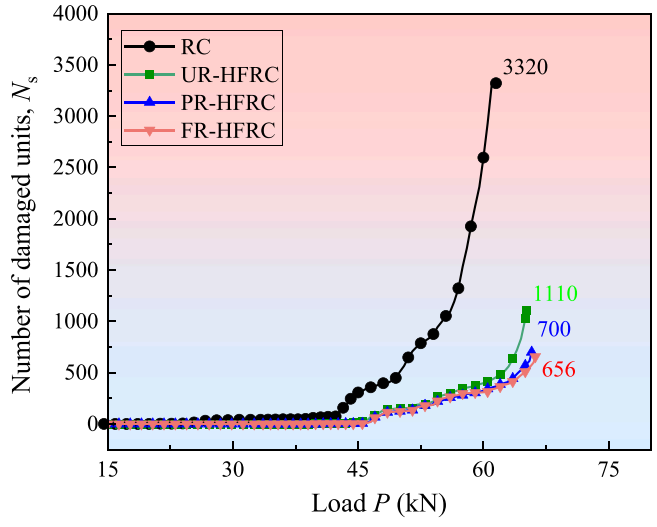

Fig. 14. The number of damaged elements in the segment ring with load *P*.

offers a superior solution to conventional RC.

4.2. Bolt stress analysis

Fig. 15 illustrates the stress distribution of bolts in the UR-HFRC segmental ring at different load levels. Due to the relatively symmetrical deformation of the tunnel, the local regions around the 7.5°, 72°, and 144° joints were enlarged to reveal the distribution of stress on the bolt body. It should be noted that while bolts in actual structures are generally considered uniformly tensioned components, in 3D FEM modeling, the interaction between the bolts and the surrounding concrete, including contact normal stress and friction, causes variations in the stress distribution along the bolts. However, the maximum stress typically occurs in the middle of the bolts rather than at the nuts. The results indicate that the bolts at the 72° joint experience higher tensile stress levels, suggesting that these locations exhibit greater internal forces. Most areas of the bolt body reach a yielding state at ultimate load level. In contrast, the bolts at the 7.5° joint exhibit only localized yielding. Moreover, the stress level at the 144° joint is lower compared to other locations, and the stress distribution is relatively uniform.

Fig. 16 illustrates the evolution of bolt stress with respect to the load

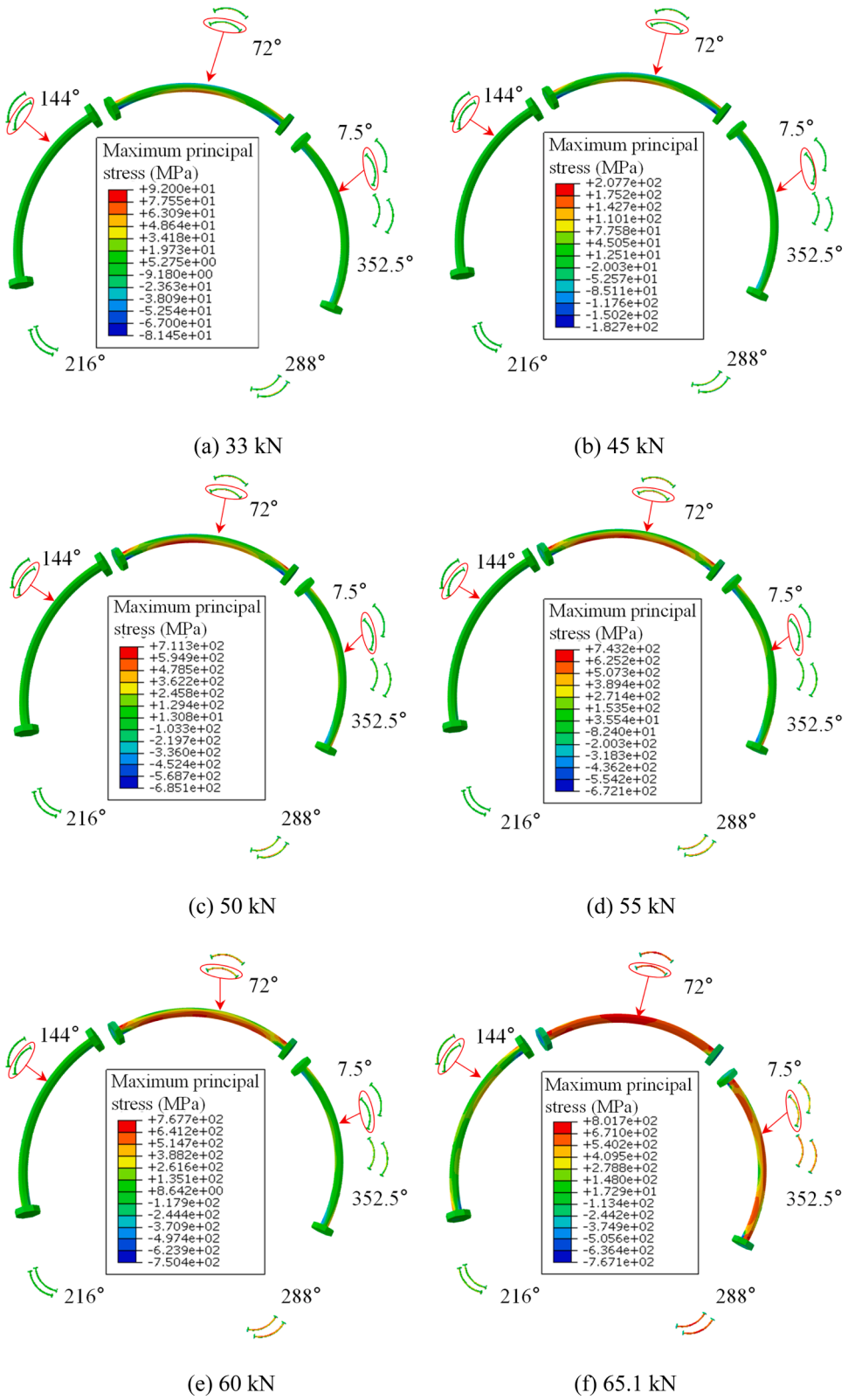

Fig. 15. The stress distribution of bolts at different load levels of the UR-HFRC segmental ring.

P, and the node where the maximum principal stress first reaches 640 MPa is selected for analysis. From Fig. 16(a) and (b), the segment ring reaches the ultimate failure phase (Phase 4), while the bolt essentially achieves its yield state. Notably, the stress states of bolts at 7.5° and 352.5° positions show asymmetric difference, and this is due to the slightly asymmetric load distribution on element nodes of the 3D model. At the 72° and 288° joints (see Fig. 16(c) and (d)), the bolt stress reaches the yield stress and then undergoes a plateau period, during which the non-yielding portions of the bolts continue to undergo plastic deformation. In contrast, at the 144° and 216° joints (see Fig. 16(e) and (f)),

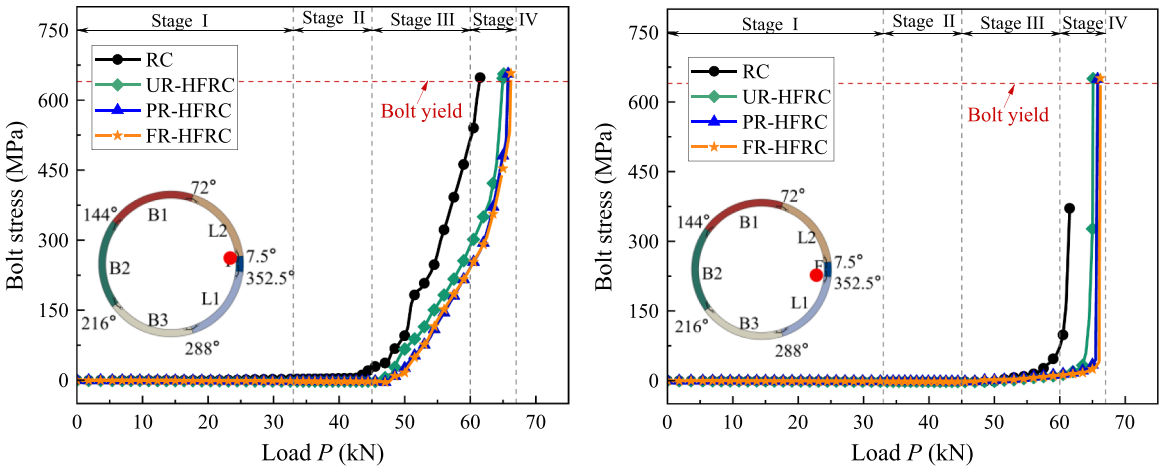

(a) 7.5° joint (b) 352.5° joint

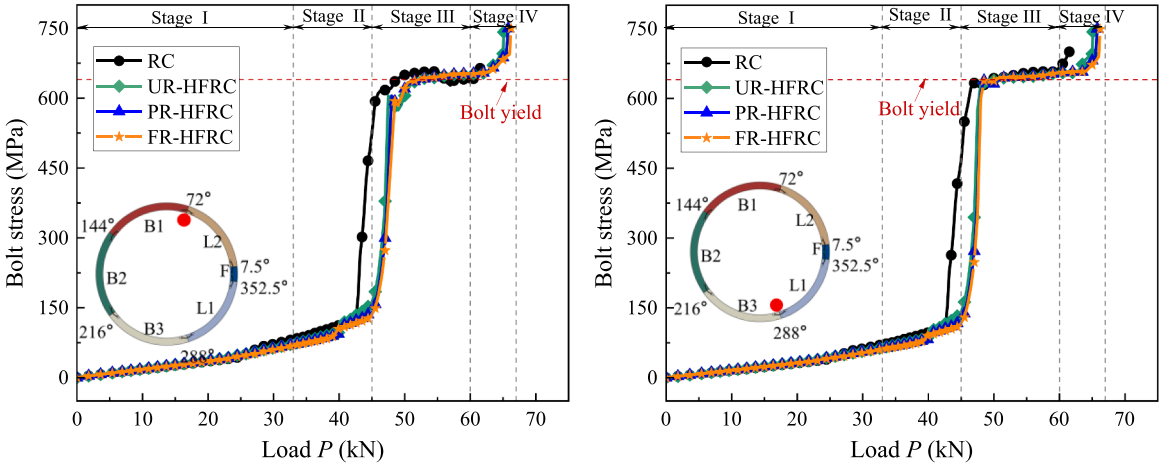

(c) 72° joint (d) 288° joint

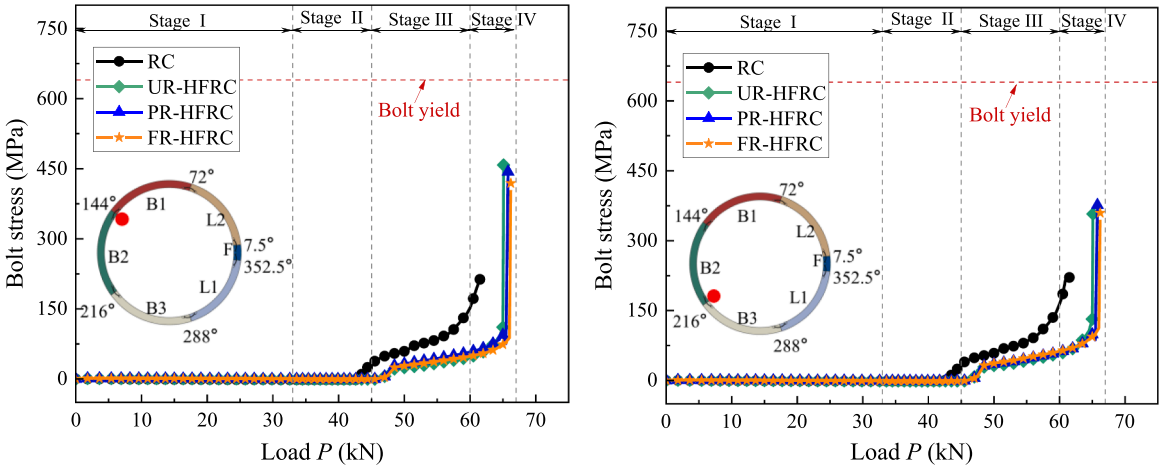

(e) 144° joint (f) 216° joint

Fig. 16. Evolution of bolt stress at joints with generalized load *P*.

the bolts do not reach yield stress. In the RC segmental ring, the bolt stresses at 144° and 216° joints reaches 213 MPa and 221 MPa, respectively, which corresponds to 33 % and 35 % of the yield stress (640 MPa). In contrast, the HFRC segmental ring exhibits higher bolt stresses at the same locations, with values of approximately 440 MPa and 360 MPa, accounting for 69 % and 56 % of the yield stress. This phenomenon indicates that HFRC enhances the cooperative interaction between the bolts and segments, thereby boosting the structural

performance of the tunnel ring lining.

4.3. Rebar stress analysis

Fig. 17 illustrates the stress evolution of steel rebar within the segment ring under the generalized load *P*, focusing on the stress at five characteristic points with the highest maximum principal stress levels. The characteristic point locations in the figures are indicated by red dots, with red dots on the inner side of the tunnel ring representing the inner rebar, while those on the outer side represent the outer rebar. As shown in the Fig. 17, during the initial elastic phase (*P* below 40 kN) the rebar stresses of the three types of segments do not show significant differences, but these differences become more significant gradually in the following elastic-plastic phase. The growth of rebar stress primarily occurs during the structure hardening phase-3 and the ultimate failure phase-4. These characteristic points are located in areas where extensive cracks occur (see Fig. 15). During these two phases, the concrete damage develops rapidly, leading to significant cracking, and tensile stress gradually transfers from the cracked concrete to the rebar. It is evident that the stress on the rebar in all types of segments does not reach the yield level (400 MPa). Notably, in the RC segment, the rebar stress near the joint locations of 72° and 288° peaks at 78 % and 74 % of the yield stress, respectively. This indicates that the reinforcement rebars are underutilized and has not fully realized its load-bearing potential in this failure mode.

Further analysis reveals that the steel stress in the RC ring is significantly higher than that in the HFRC segment ring, suggesting that HFRC undertakes more tensile stress and thus reduces the rebar stress level. Additionally, Fig. 17(a) and (e) demonstrate a similar trend in stress growth, where the rebar stress only begins to increase significantly after the tunnel ring exceeds its elastic-plastic limit, and this increase occurs at a relatively slow rate. In contrast, the rebar stress in Fig. 17(b), (c), and (d) exhibits a rapid growth state, particularly notable in the RC segment ring. Finally, the locations of peak rebar strain vary by segment within a tunnel ring, as those of segments B1, B3, L2, and L1 lie near the joints, while that of B2 is in the middle. These rebar peak strain points also align with the formation of plastic hinges in the ultimate limit state as discussed in Section 5.1.

4.4. Structural behavior of segmental ring

To evaluate the overall structural deformation response, four successive structure deformation phases and three key indicators characterizing structure bearing capacity are defined in Section 4.1, including the elastic limit, elastoplastic limit, and bearing capacity limit respectively. The load-displacement result curves of the segment rings are illustrated in Fig. 18, with the key structural capacity indicators marked. As shown in the results, the HFRC segment significantly boosts the elastic limit of the ring lining compared to the RC segment. This suggests that the incorporation of fibers enhances the lining's capacity to resist initial cracking, which is consistent with the findings of Meng et al. [29] and Chiaia et al. [30]. The elastoplastic limits of the four types of segment rings are very close, and this is due to the redistribution of structural internal forces after crack initiation. Bolts at joint exhibit more significant stress growth and determine the overall structural deformation. Furthermore, it can be shown in Fig. 18 that HFRC not only contributes to boosting the bearing capacity limits, but also reduces the corresponding deformations (and hence an increased stiffness level) of the segment rings compared to RC, which is consistent with the findings reported by Liu et al. [50].

4.4.1. Bearing capacity

The load-bearing capacity limit of the segment structure is defined as the maximum generalized load *P* that the structure can withstand before losing stability or reaching its ultimate failure phase. Fig. 19 illustrates the bearing capacity limits of four types of segment linings. It is evident that HFRC improves the load-bearing capacity of segment lining, with the average capacity of HFRC segments 6% higher than that of RC segments. This improvement is attributed to the higher tensile strength and crack resistance of HFRC compared to plain concrete, which helps suppress crack propagation and thereby increases the overall bearing capacity. In addition, both PR-HFRC and FR-HFRC segmental linings exhibit slightly increased load bearing capacity compared to the UR-HFRC segment, indicating a synergistic effect of steel rebars and fibers in enhancing the overall mechanical performance of the segment ring lining. However, the marginal improvement from PR-HFRC to FR-HFRC types suggests a diminishing contribution of additional reinforcement rebar beyond a certain threshold level, since the maximum bearing capacity is more determined by other components, such as the joint bolts that connect the segments.

4.4.2. Structure stiffness

The initial stiffness of the segmental ring lining is defined as the slope between the generalized load *P* at the elastic-plastic limit point and the coordinate origin, while the subsequent stiffness is defined as the slope between the elastic-plastic limit point and the ultimate bearing capacity limit, as illustrated in Fig. 18. Fig. 20 illustrates the initial and subsequent stiffnesses of RC and HFRC segment linings. Analysis reveals that the initial stiffness of FR-HFRC is approximately 2.4% higher than that of RC, whereas UR-HFRC's initial stiffness is slightly lower (less than 1%) than that of RC. In terms of subsequent stiffness, FR-HFRC shows an increase of 53% over RC, and PR-HFRC is 43% higher than RC. These results indicate that while the combination of fibers and steel has a minimal impact on initial stiffness, it significantly enhances the subsequent stiffness when structure behaves plastically, particularly effectively minimize the deformation before final failure phase.

5. Discussion and limitations

5.1. Failure mechanism

The initiation and evolution of plastic hinge within the segmental ring helps describe and explain the progressive failure mechanism of tunnel segment rings [64]. The emergence of the elastic-plastic limit in the segment ring implies the initial formation of a plastic hinge, indicating that the structure has reached its yield point. The deformation extent defining this yield points is mostly determined based on experiments. For instance, Gao et al. [65] identified the ratio of the horizontal convergence at the first yield point to the outer diameter of the tunnel as a deformation control value, which is approximately 8‰. In this study, the same deformation control value is defined and set as 7‰. After the first plastic hinge occurs at the initial yielding point, more plastic hinges occur progressively during the subsequent hardening phase. As the segment ring features a third-order hyperstatic structure, the formation of four plastic hinges results in significant deformations, leading to a decline in structural stability and a rapid loss of load-bearing capacity.

Within a segmental ring, the joint acts as a discontinuous section with a lower cross-section stiffness than that of the concrete segment. For example, the flexural stiffness of RC segments at the ultimate state under positive and negative bending moments is calculated as 27.9 and 19 times greater, respectively, than that of the longitudinal joints [64]. Accordingly, more significant deformations occur at the joint, leading to an elevated tensile stress in the bolts, and a further loading step may easily cause bolt failure or crush the nearby concrete in the compression zone of the joint cross-section. Therefore, plastic hinge is more likely to form initially at joints. In addition, excessive bending moments on the curved segment body can cause yielding of internal rebars and the crushing of concrete in the compression zone and eventual yielding of the entire segment cross-section, indicating formation of additional plastic hinge.

Fig. 21 illustrates the sequence and locations of plastic hinge formation in the segment ring upon reaching its ultimate failure state. The

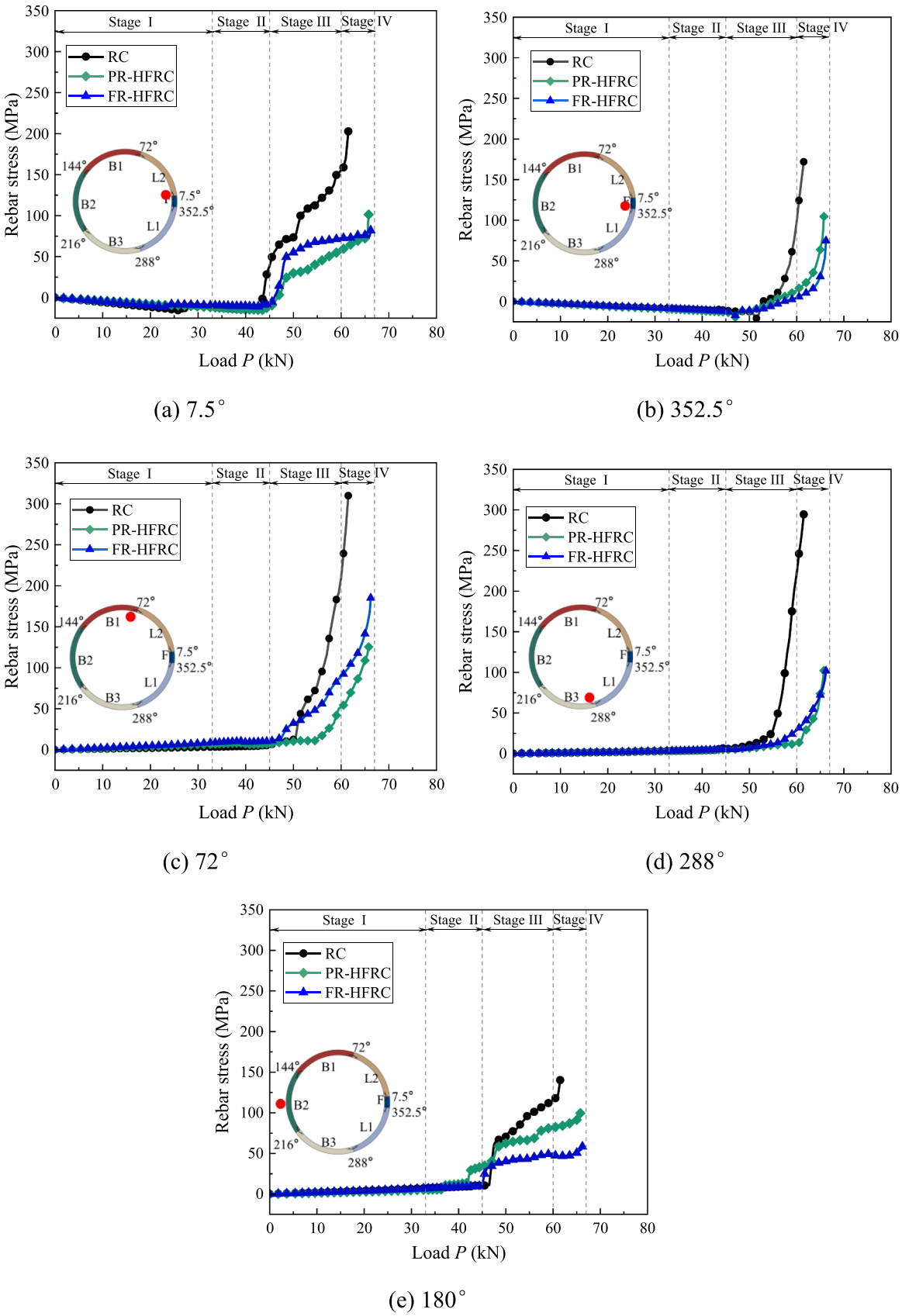

Fig. 17. Evolution of reinforcing rebar stress with generalized load *P*.

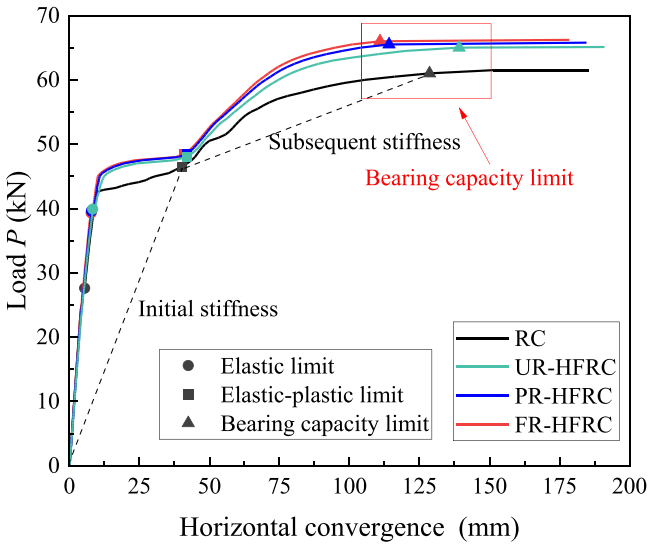

Fig. 18. Horizontal convergence deformation evolution with generalized load P.

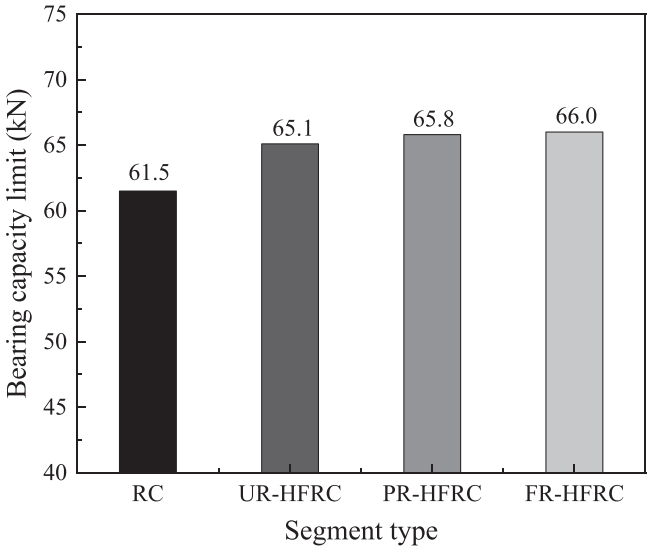

Fig. 19. Bearing capacity limits magnitudes of four types of segment linings.

RC segment ring develops four joint plastic hinges, resulting in a loss of stability and achieving the maximum bearing capacity limit. Correlating with Fig. 13(a), significant crack formation occurs near the 72° and 288° joints, where these connections completely lose stability, leading to structural failure. Additionally, a higher number of cracks and greater rebar stress at the 180° location indicate the imminent formation of a plastic hinge. In the UR-HFRC segment ring, three joint plastic hinges and one segment plastic hinge are formed. The occurrence of the segment plastic hinge is attributed to the absence of rebar, which causes the segment to reach yielding after crack formation. In contrast, the PR-HFRC and FR-HFRC segment rings exhibit four joint plastic hinges, indicating that even at the bearing capacity limit, the segments do not yield. This suggests that the hybrid HFRC-reinforcement solution enhances the load-bearing capacity of the segments, effectively utilizing the performance of the bolts.

5.2. Serviceability aspect

Tunnel segments must meet not only the ultimate limit state requirements but also serviceability requirements, such as watertightness and durability, which are typically ensured by controlling crack width to a general limit of 0.2 mm according to Chinese design criteria. However, due to the inherent limitations of the concrete constitutive model, the 3D FEM in this study cannot directly quantify the crack width. Despite the missing crack-width information, it is meaningful to utilize other indicators to evaluate the structural serviceability limit state (SLS) of the four segment types. Chinese structural design code for shield tunnel (GB/T 51438–2021) [66] proposes convergence deformation as a key criterion to ensure serviceability limit requirements. It is required that the horizontal convergence deformation of tunnel transverse cross-section be controlled within 0.3% of the outer diameter, namely 18 mm in this study.

As shown in Fig. 18, with the constraint horizontal convergence limit of 18 mm, the corresponding differential surcharge load *P* for all HFRC segment types lies about 47 kN, while the *P* for RC segment is about 43 kN, which implies that the addition of fiber enhances the segment ling's bearing capacity level under the considered maximum allowable convergence associated with serviceability requirements. Additionally, when the segment lining behaves following elastic-plastic phase (Stage 2), it is only at the initial time of phase that the horizontal convergence exhibit below the stipulated limit. Notably, it further develops rapidly even under a small increase of differential surcharge *P*, and after the very initial time the convergence deformation quickly exceeds the limit of 18 mm, implying that once entering the elastic-plastic phase, the four types of segment linings are likely to exhibit an excessive horizontal convergence beyond the serviceability limit.

5.3. Recommendations for design

HFRC exhibits advantages in enhancing crack resistance and energy dissipation capacity, and integrating HFRC with reinforcement offers great potential in boosting tunnel segment's resistance to adverse surcharge loads. Based on the findings in this study, several design optimization recommendations can be further proposed, focusing on three key aspects: (1) Optimal reinforcement configuration: The marginal improvement in bearing capacity from PR-HFRC to FR-HFRC suggests that an excessive increase in reinforcement ratio beyond a certain threshold (e.g., 0.79% in PR-HFRC) may not yield proportional benefits. This recommends adopting a balanced reinforcement ratio (e.g., 0.8–1.0 %) combined with hybrid fibers to achieve cost-effective crack resistance and load-bearing capacity without material wastage; (2) Joint design optimization: The formation of plastic hinges predominantly at segment joints in HFRC linings underscores the need for enhanced joint detailing. For instance, it is suggested that increasing bolt tensile capacity or incorporating fiber reinforcement around joint zones mitigate stress concentrations and delay bolt yielding, thereby improving overall structural performance; (3) Fiber dosage and type: The study utilized a hybrid combination of 0.3% macro hooked-end steel fibers and 0.2% micro straight steel fibers, which effectively enhanced tensile strength and crack resistance. This fiber mixing ratio can serve as a starting point for HFRC tunnel linings, with adjustments based on specific project requirements (e.g., higher fiber dosages for deeper tunnels with greater surcharge loads).

5.4. Limitations of this study

This study investigates the mechanical properties and progressive failure mechanisms of four types of segment linings, focusing on HFRC through 3D finite element modeling. Several limitations exist in the current simulation. Although the 3D numerical model has been validated against full-scale loading tests for RC segment linings, no such validation exists for HFRC segments. Conducting further load tests on HFRC linings would provide valuable data to guide their design and application. In addition, the serviceability criteria are not well checked due to a lack of crack width information associated with the inherent

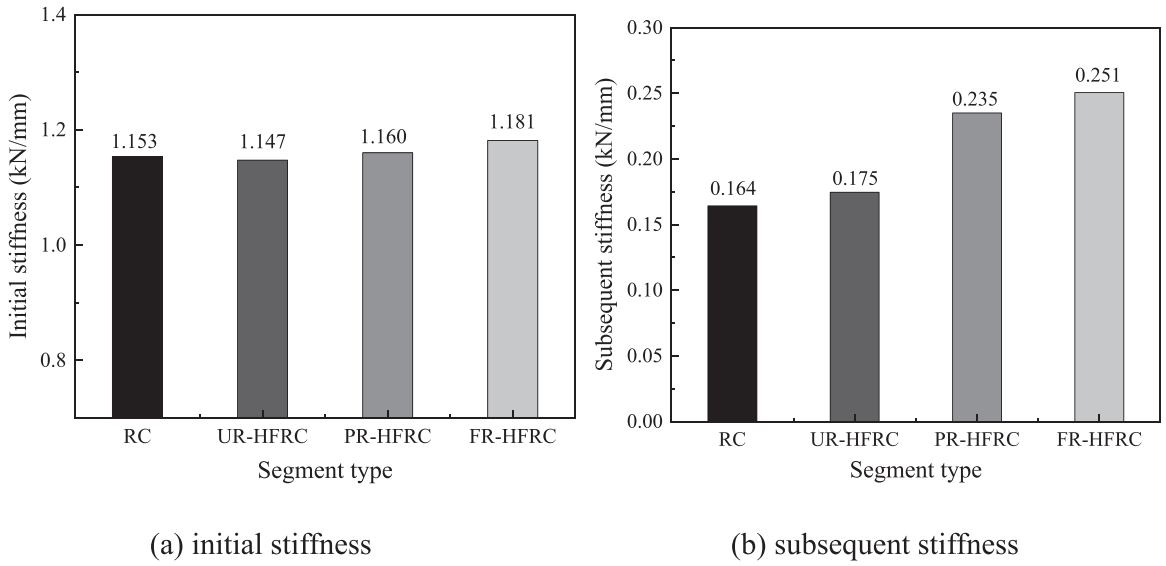

(a) initial stiffness (b) subsequent stiffness

Fig. 20. Comparison of the structural stiffnesses of four types of segment linings.

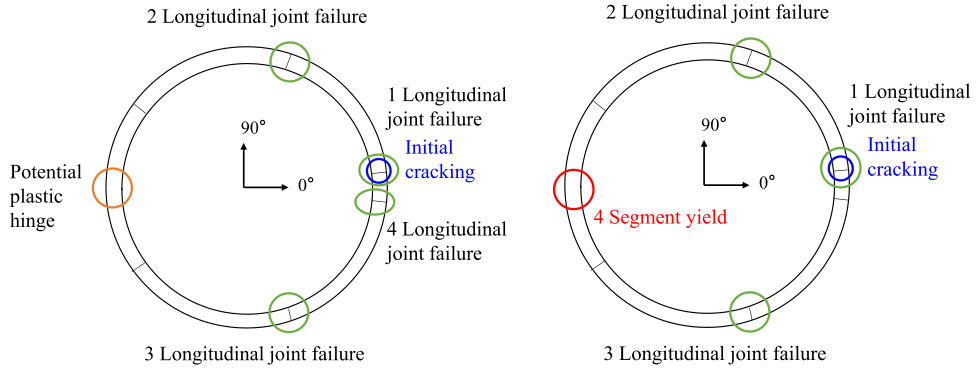

(a) RC segment (b) UR-HFRC segment

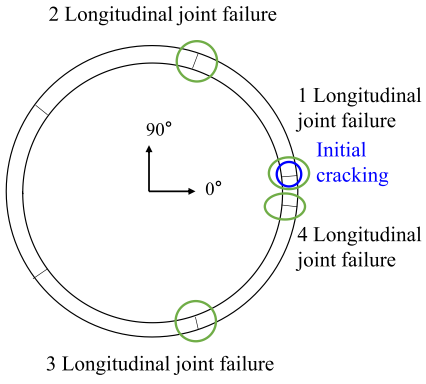

(c) PR-HFRC/ FR-HFRC segment

Fig. 21. Distribution of plastic hinges in the bearing capacity limit.

limitations of the concrete constitutive model and the 3D FEA model in this study. Future research on crack width evolution of segment lining is recommended to be conducted by utilizing other numerical simulation methods or physical model tests. Finally, the current study focuses on a single ring, overlooking the longitudinal spatial effects of multiple rings, such as inter-ring joint behavior. Future research should address these limitations by incorporating varying fiber and reinforcement ratios, conducting full-scale tests on HFRC linings, investigating crack-width information and taking into account multi-ring configurations to gain a more holistic understanding of HFRC performance for practical engineering applications.

6. Conclusions

This study investigates the structural behavior and progressive failure characteristics of four types of shield tunnel segments: RC, UR-HFRC, PR-HFRC, and FR-HFRC. The analysis is based on a detailed 3D FEM. The following key conclusions are drawn:

(1) The refined 3D FEM, which incorporates key structural components of the segment—such as manholes, bolts, and reinforcement rebars—along with appropriate boundary conditions and material parameters. It was validated as sufficiently accurate in simulating the structural response of segment rings under surcharge loads. The simulation results for the RC segment lining closely aligned with observations from the full-scale load test, particularly in terms of failure modes and damage patterns.

(2) The numerical simulation results demonstrate that all four types of segment rings exhibit a progressive structural response under surcharge loads, transitioning through the elastic, elastoplastic, hardening, and ultimate failure phases. However, each segment type exhibits distinct behaviors during these deformation phases .

(3) The FR-HFRC segment ring exhibits the highest ultimate bearing capacity among the four segment types, showing a 7.3% improvement over RC. While the influence of HFRC on the initial stiffness in the elastic phase is limited, the subsequent stiffness in the hardening phase for PR-HFRC and FR-HFRC is improved by 43% and 53%, respectively, compared to RC. This demonstrates the effective contribution of the combined HFRC and rebar configuration in enhancing the structural subsequent stiffness.

(4) For segments with rebars (RC, PR-HFRC, FR-HFRC), the reinforcement rebars effectively prevent cross-sectional yielding of the segments. However, this comes at the cost of the formation of four successive plastic hinges at the joints once the ring structure reaches the ultimate failure phase. In contrast, the UR-HFRC segment ring develops plastic hinges both within the segments and at the joints. Thus, the inclusion of reinforcement rebars alters the ultimate failure modes of HFRC segment rings.

HFRC exhibits significant potential to enhance the performance of segmental tunnel linings, particularly by improving structural crack resistance and load-bearing capacity. Through the optimization of material configurations, HFRC offers a promising approach to tunnel lining design that is not only efficient and cost-effective but also environmentally friendly.

CRediT authorship contribution statement

Zhang Xuehui: Writing – review & editing, Writing – original draft, Methodology, Investigation, Formal analysis. **Li Yingpeng:** Writing – original draft, Visualization, Methodology, Investigation, Formal analysis, Data curation. **Bao Xiaohua:** Writing – review & editing, Supervision, Methodology, Investigation, Funding acquisition, Conceptualization. **Cui Hongzhi:** Supervision, Project administration, Methodology. **Chen Xiangsheng:** Supervision, Methodology, Funding acquisition. **Wu Xianlong:** Visualization, Validation, Data curation.

Declaration of Competing Interest

The authors declare that they have no known competing financial interests or personal relationships that could have appeared to influence the work reported in this paper.

Acknowledgment

This work was financially supported by the National Key R&D Program of China (Grant No. 2024YFF0507902), the National Natural Science Foundation of China (Grant No. 52090084), and the Shenzhen Science and Technology Program (Grant No. KQTD20200909113951005 & JCYJ20220531101214031).

Data availability

Data will be made available on request.

References

[1] Broere W. Urban underground space: solving the problems of today's cities. Tunn Undergr Space Technol 2016;55:245–8. https://doi.org/10.1016/j.tust.2015.11.012.
[2] Cui J, Broere W, Lin D. Underground space utilisation for urban renewal. Tunn Undergr Space Technol 2021;108:103726. https://doi.org/10.1016/j.tust.2020.103726.
[3] Xu D, Zhang X, Chen W, Jiang X, Liu Z, Bai Y. Utilisation of the deep underground space in Shanghai. Proc Inst Civ Eng -Munic Eng 2019;172(4):218–23. https://doi.org/10.1680/jmuen.18.00029.
[4] Zhang X, Zhu H, Jiang X, Broere W. Distributed fiber optic sensors for tunnel monitoring: a state-of-the-art review. J Rock Mech Geotech Eng 2024. https://doi.org/10.1016/j.jrmge.2024.01.008.
[5] Wang D, Zhu H, Zhang X, Huang J, Yan Z, Tan D, Lin S. Structural behavior of triple-layer composite lining of a water conveyance tunnel: insight from full-scale loading tests. J Rock Mech Geotech Eng 2024;2024. https://doi.org/10.1016/j.jrmge.2024.11.025.
[6] Xu S, Ma E, Lai J, Yang Y, Liu H, Yang C, Hu Q. Diseases failures characteristics and countermeasures of expressway tunnel of water-rich strata: a case study. Eng Fail Anal 2022;134:106056. https://doi.org/10.1016/j.engfailanal.2022.106056.
[7] Yue Y, Zhang S, Liu H, Hong F, Liu C, Cui J, Du Y. Damage mechanism of a shield tunnel with cavities behind the concrete lining: an insight from a scaled model test. Tunn Undergr Space Technol 2024;153:105998. https://doi.org/10.1016/j.tust.2024.105998.
[8] Zhang G, Liu G, Lu Z, Yan C, Xu L, Gao Q, Zhou Y. Evaluation method for health state of highway tunnel structure based on adaptive comprehensive weighting. Eng Fail Anal 2024;163:108597. https://doi.org/10.1016/j.engfailanal.2024.108597.
[9] Chen J, Hu T, Hu X, Jia K. Study on the influence of crack depth on the safety of tunnel lining structure. Tunn Undergr Space Technol 2024;143:105470. https://doi.org/10.1016/j.tust.2023.105470.
[10] Zhang X, Long L, Broere W, Bao X. Smart sensing of concrete crack using distributed fiber optics sensors: current advances and perspectives. Case Stud Constr Mater 2025;22:e04493. https://doi.org/10.1016/j.cscm.2025.e04493.
[11] Li C, Chen Q, Wang R, Wu M, Jiang Z. Corrosion assessment of reinforced concrete structures exposed to chloride environments in underground tunnels: theoretical insights and practical data interpretations. Cem Concr Compos 2020;112:103652. https://doi.org/10.1016/j.cemconcomp.2020.103652.
[12] Gong C, Cheng M, Ge Y, Song J, Zhou Z. Leakage mechanisms of an operational underwater shield tunnel and countermeasures: a case study. Tunn Undergr Space Technol 2024;152:105892. https://doi.org/10.1016/j.tust.2024.105892.
[13] Zhang X, Zhu H, Jiang X, Broere W. Designing a distributed sensing network for structural health monitoring of concrete tunnels: a case study. Struct Control Health Monit 2024;2024(1):6087901. https://doi.org/10.1155/2024/6087901.
[14] Ezazi M, Hossaini MF, Sheikhmali R, Khosrotash M, Teshnizi ES, O'Kelly BC. Assessment of steel-fiber-reinforced segmental lining of Chamshir water conveyance tunnel, Iran: integrating laboratory experiments, field observations, and numerical analysis. Case Stud Constr Mater 2024;20:e03144. https://doi.org/10.1016/j.cscm.2024.e03144.
[15] Wang Q, Geng P, Li P, He D, Shen H. Failure analysis of circumferential joints and preferable bolt form of shield tunnel under normal fault dislocation. Tunn Undergr Space Technol 2024;146:105648. https://doi.org/10.1016/j.tust.2024.105648.
[16] Bao X, Wu X, Zhang X, Shen J, Chen X, Dang P, Cui H. Mechanical behaviours of concrete segmented tunnel considering the effects of grouting voids — a 3D numerical simulation. Case Stud Constr Mater 2025;22:e04370. https://doi.org/10.1016/j.cscm.2025.e04370.
[17] Zhao Z, Cui J, Liu C, Liu H, ur, Rehman M, Chen W, Peng Z. Seismic damage characteristics of large-diameter shield tunnel lining under extreme-intensity earthquake. Soil Dyn Earthq Eng 2023;171:107958. https://doi.org/10.1016/j.soildyn.2023.107958.
[18] Tabrizikahou A, Kuczma M, Czaderski C, Shahverdi M. From experimental testing to computational modelling: a review of shape memory alloy fiber-reinforced concrete composites. Compos Pt B-Eng 2024:111530. https://doi.org/10.1016/j.compositesb.2024.111530.
[19] Zhang H, Wu Z, Hu X, Ouyang X, Zhang Z, Banthia N, Shi C. Design, production, and properties of high-strength high-ductility cementitious composite (HSHDCC): a review. Compos Pt B-Eng 2022;247:110258. https://doi.org/10.1016/j.compositesb.2022.110258.
[20] Zhang P, Wang C, Gao Z, Wang F. A review on fracture properties of steel fiber reinforced concrete. J Build Eng 2023;67:105975. https://doi.org/10.1016/j.jobe.2023.105975.
[21] Wang Z, Wang P, Zhu F. Synergy effect of hybrid steel-polyvinyl alcohol fibers in engineered cementitious composites: fiber distribution and mechanical performance. J Build Eng 2022;62:105348. https://doi.org/10.1016/j.jobe.2022.105348.
[22] Banthia N, Majdzadeh F, Wu J, Bindiganavile V. Fiber synergy in Hybrid Fiber Reinforced Concrete (HyFRC) in flexure and direct shear. Cem Concr Compos 2014;48:91–7. https://doi.org/10.1016/j.cemconcomp.2013.10.018.

[23] Banthia N, Majdzadeh F, Wu J, Bindiganavile V. Fiber synergy in Hybrid Fiber Reinforced Concrete (HyFRC) in flexure and direct shear. Cem Concr Compos 2014;48:91–7. https://doi.org/10.1016/j.cemconcomp.2013.10.018.

[24] Carmona S, Molins C, Aguado A, Mora F. Distribution of fibers in SFRC segments for tunnel linings. Tunn Undergr Space Technol 2016;51:238–49. https://doi.org/10.1016/j.tust.2015.10.040.

[25] Gong C, Ding W, Mosalam KM, Günay S, Soga K. Comparison of the structural behavior of reinforced concrete and steel fiber reinforced concrete tunnel segmental joints. Tunn Undergr Space Technol 2017;68:38–57. https://doi.org/10.1016/j.tust.2017.05.010.

[26] Nehdi ML, Abbas S, Soliman AM. Exploratory study of ultra-high performance fiber reinforced concrete tunnel lining segments with varying steel fiber lengths and dosages. Eng Struct 2015;101:733–42. https://doi.org/10.1016/j.engstruct.2015.07.012.

[27] Yang K, Yan Q, Zhang C. Three-dimensional mesoscale numerical study on the mechanical behaviors of SFRC tunnel lining segments. Tunn Undergr Space Technol 2021;113:103982. https://doi.org/10.1016/j.tust.2021.103982.

[28] Nogales A, de la Fuente A. Crack width design approach for fibre reinforced concrete tunnel segments for TBM thrust loads. Tunn Undergr Space Technol 2020;98:103342. https://doi.org/10.1016/j.tust.2020.103342.

[29] Meng G, Gao B, Zhou J, Cao G, Zhang Q. Experimental investigation of the mechanical behavior of the steel fiber reinforced concrete tunnel segment. Constr Build Mater 2016;126:98–107. https://doi.org/10.1016/j.conbuildmat.2016.09.028.

[30] Chiaia B, Fantilli AP, Vallini P. Combining fiber-reinforced concrete with traditional reinforcement in tunnel linings. Eng Struct 2009;31(7):1600–6. https://doi.org/10.1016/j.engstruct.2009.02.037.

[31] Conforti A, Trabucchi I, Tiberti G, Plizzari GA, Caratelli A, Meda A. Precast tunnel segments for metro tunnel lining: a hybrid reinforcement solution using macro-synthetic fibers. Eng Struct 2019;199:109628. https://doi.org/10.1016/j.engstruct.2019.109628.

[32] Gholami E, Afshin H, Basim MC, Sharghi M. Ultra-high performance recycled steel fiber reinforced concrete segments under the thrust force of TBM jacks and their environmental potentialities. Structures 2023;47:2465–84. https://doi.org/10.1016/j.istruc.2022.12.051.

[33] Trabucchi I, Tiberti G, Plizzari GA. A parametric numerical study on the behavior of large precast tunnel segments during TBM thrust phase. Eng Struct 2021;241:112253. https://doi.org/10.1016/j.engstruct.2021.112253.

[34] Taerwe, L., Matthys, S., 2013. Fib model code for concrete structures 2010. http://hdl.handle.net/1854/LU-4255771.

[35] Yan ZG, Shen Y, Zhu HH, Li XJ, Lu Y. Experimental investigation of reinforced concrete and hybrid fibre reinforced concrete shield tunnel segments subjected to elevated temperature. Fire Saf J 2015;71:86–99. https://doi.org/10.1016/j.firesaf.2014.11.009.

[36] Abbas S, Nehdi ML. Mechanical behavior of ultrahigh-performance concrete tunnel lining segments. Materials 2021;14(9):2378. https://doi.org/10.3390/ma14092378.

[37] Liu M, Jia S, He X. A quota-based GHG emissions quantification model for the construction of subway stations in China. J Clean Prod 2018;198:847–58. https://doi.org/10.1016/j.jclepro.2018.07.067.

[38] Caratelli A, Meda A, Rinaldi Z. Design according to MC2010 of a fibre-reinforced concrete tunnel in Monte Lirio, Panama. Struct Concr 2012;13(3):166–73. https://doi.org/10.1002/suco.201100034.

[39] Liu X, Zhang Y, Bao Y. Full-scale experimental investigation on stagger effect of segmental tunnel linings. Tunn Undergr Space Technol 2020;102:103423. https://doi.org/10.1016/j.tust.2020.103423.

[40] Zhou L, Shen Y, Guan L, Yan Z, Sun W, Li Y. Full-scale experiment for segmental linings of deep-buried shield tunnels bearing high inner water pressure: comparison of mechanical behaviors of continuous-and stagger-jointed structures. Undergr Space 2023;8:252–66. https://doi.org/10.1016/j.undsp.2022.03.005.

[41] Tengilimoglu O, Akyuz U. Experimental study on hybrid precast tunnel segments reinforced by macro-synthetic fibres and glass fibre reinforced polymer bars. Tunn Undergr Space Technol 2020;106:103612. https://doi.org/10.1016/j.tust.2020.103612.

[42] Xu H, Wang Z, Shao Z, Jin H, Li Z, Jiang X, Cai L. Experimental study on crack features of steel fiber reinforced concrete tunnel segments subjected to eccentric compression. Mater Today Commun 2020;25:101349. https://doi.org/10.1016/j.mtcomm.2020.101349.

[43] Meda A, Rinaldi Z, Spagnuolo S, De Rivaz B, Giamundo N. Hybrid precast tunnel segments in fiber reinforced concrete with glass fiber reinforced bars. Tunn Undergr Space Technol 2019;86:100–12. https://doi.org/10.1016/j.tust.2019.01.016.

[44] Domingo M, Ramos G, Aparicio ÁC. Use of fiber reinforced concrete in bridges–Metrorrey Line 2 case study. Eng Struct 2023;276:115373. https://doi.org/10.1016/j.engstruct.2022.115373.

[45] de Andrade GG, de Figueiredo AD, Galobardes I, da Silva MA, de la Fuente A, Bitencourt Jr LA. Experimental and numerical investigation of flexural behavior of precast tunnel segments with hybrid reinforcement. Tunn Undergr Space Technol 2024;154:106094. https://doi.org/10.1016/j.tust.2024.106094.

[46] Liu X, Zhang Y, Bao Y, Song W. Investigation of the structural effect induced by stagger joints in segmental tunnel linings: numerical explanation via macro-level structural modeling. Tunn Undergr Space Technol 2022;120:104284. https://doi.org/10.1016/j.tust.2021.104284.

[47] Chen RP, Chen S, Wu HN, Liu Y, Meng FY. Investigation on deformation behavior and failure mechanism of a segmental ring in shield tunnels based on elaborate numerical simulation. Eng Fail Anal 2020;117:104960. https://doi.org/10.1016/j.engfailanal.2020.104960.

[48] Shen Y, Ling J, Wang W, Zhu H, Yan Z. 3D numerical investigation on response of shield tunnel under combined effects of fire and structural loading. Tunn Undergr Space Technol 2022;128:104659. https://doi.org/10.1016/j.tust.2022.104659.

[49] Shen Y, Zhu H, Yan Z, Zhou L, Zhang T, Men Y, Lu Y. Thermo-mechanical analysis of fire effects on the structural performance of shield tunnels. Tunn Undergr Space Technol 2023;132:104885. https://doi.org/10.1016/j.tust.2022.104885.

[50] Liu X, Sun Q, Song W, Bao Y. Numerical modeling and parametric study of hybrid fiber-rebar reinforced concrete tunnel linings. Eng Struct 2022;251:113565. https://doi.org/10.1016/j.engstruct.2021.113565.

[51] Lu Y. Full-scale Model Test of Shield Tunnel Segment and Simulation Analysis of Circumferential Joint. Beijing: China Academy of Railway Sciences; 2019 (in Chinese).

[52] GB 50010-2010, 2010. Code for Design of Concrete Structures. Ministry of Housing and Urban-Rural Development of Peoples's Republic of China. (in Chinese).

[53] Liu C, Peng Z, Cui J, Huang X, Li Y, Chen W. Development of crack and damage in shield tunnel lining under seismic loading: refined 3D finite element modeling and analyses. Thin-Walled Struct 2023;185:110647. https://doi.org/10.1016/j.tws.2023.110647.

[54] Bao X, Li Y, Chen X, Yang H, Cui H. Experimental investigation on axial compressive and splitting tensile behaviour of reinforced concrete with a low content of hybrid steel fibres. Constr Build Mater 2024;428:136315. https://doi.org/10.1016/j.conbuildmat.2024.136315.

[55] Li Y, Bao X, Chen X, Zhang R, Cui H. Fracture behaviour of hybrid fibre reinforced concrete with a low fibre content considering the form of layered beams. Constr Build Mater 2024:137632. https://doi.org/10.1016/j.conbuildmat.2024.137632.

[56] Bao X, Li Y, Chen X, Yang H, Cui H. Investigation on the flexural behaviour and crack propagation of hybrid steel fibre reinforced concrete with a low fibre content for tunnel structures. Constr Build Mater 2024;417:135253. https://doi.org/10.1016/j.conbuildmat.2024.135253.

[57] Vandewalle L, Nemegeer D, Balazs L, Barr B, Barros J, Bartos P, Walraven J. RILEM TC 162-TDF: test and design methods for steel fibre reinforced concrete'-sigma-epsilon-design method-Final Recommendation. Mater Struct 2003;36(262):560–7. ⟨https://orbit.dtu.dk/en/publications/rilem-tc-162-tdf-test-and-design-methods-for-steel-fibre-reinforc⟩.

[58] Su D, Chen W, Wang X, Huang M, Pang X, Chen X. Numerical study on transverse deformation characteristics of shield tunnel subject to local soil loosening. Undergr Space 2022;7(1):106–21. https://doi.org/10.1016/j.undsp.2021.07.001.

[59] Chen R, Chen S, Wu H, Liu Y, Meng F. Investigation on deformation behavior and failure mechanism of a segmental ring in shield tunnels based on elaborate numerical simulation. Eng Fail Anal 2020;117:104960. https://doi.org/10.1016/j.engfailanal.2020.104960.

[60] Zheng G, Pang X, Wang K. Failure mechanism of shield tunnel based on full-scale experiment and analysis of longitudinal joint's outboard deformation (in chinese) Tunn Constr 2021;41(2):165–71. https://doi.org/10.3973/j.issn.2096-4498.2021.S2.021.

[61] Dassault Systèmes. 2021. ABAQUS SIMULIA User Assistance 2021. Dassault Systèmes Simulia Corp. ⟨https://help.3ds.com/2021/English/DSSIMULIA_Established/SIMACAECAERefMap/simacae-c-topmenubar.htm?contextscope=all&redirect_lang=English⟩.

[62] Moradloo AJ, Adib A, Pirooznia A. Damage analysis of arch concrete dams subjected to underwater explosion. Appl Math Model 2019;75:709–34. https://doi.org/10.1016/j.apm.2019.04.064.

[63] Du XL, Jin L, Ma GW. Numerical simulation of dynamic tensile-failure of concrete at meso-scale. Int J Impact Eng 2014;66:5–17. https://doi.org/10.1016/j.ijimpeng.2013.12.005.

[64] Liang K, Feng K, Zhang L, He C, Su A, Guo W. Failure mechanism of underwater shield tunnel: an experimental and theoretical study. Tunn Undergr Space Technol 2023;137:105155. https://doi.org/10.1016/j.tust.2023.105155.

[65] Gao B, Chen R, Wu H, Zhang C, Fan M, Xiao C. Investigation of mechanical failure performance of a large-diameter shield tunnel segmental ring. J Zhejiang Univ -SCI A 2024;25(5):411–28. https://doi.org/10.1631/jzus.A2300446.

[66] Ministry of Housing and Urban-Rural Development of the People's Republic of China, 2021. Standard for design of shield tunnel engineering (GB/T 51438–2021). Beijing: China Architecture & Building Press..